Orographic Influence on a Drifting Cyclone

YUH-LANG LIN, JONGIL HAN, AND DAVID W. HAMILTON

Department of Marine, Earth and Atmospheric Sciences, North Carolina State University, Raleigh, North Carolina

CHING-YUANG HUANG

Department of Atmospheric Science, National Central University, Chung-Li, Taiwan

(Manuscript received 10 April 1996, in final form 16 April 1998)

ABSTRACT

In this study, a primitive equation numerical model is adopted to investigate the orographic influence on a drifting cyclone over an idealized topography similar to that of Taiwan. For a cyclone propagating from the east and impinging on the central portion of the mountain, a northerly surface jet tends to form upstream of the mountain between the primary cyclone and the mountain due to blocking and channeling effects. Two pressure ridges and one trough are also produced. When the cyclone approaches the mountain, the low-level vorticity and low pressure centers decelerate and turn southward upstream of the mountain due to orographic blocking. At the same time, the upstream low-level vorticity is blocked by the mountain. The abrupt increase of surface vorticity and the contraction of cyclone scale on the lee side are explained by the generation of new potential vorticity (PV) due to wave breaking associated with the severe downslope wind and hydraulic jump. The generation of this new PV is evidenced by the transition from the regime dominated by flow splitting to the regime dominated by wave breaking and the dominance of mixing and diffusion term in the vorticity and PV budgets. At this stage, the cyclone and low pressure centers appear to accelerate or jump over the mountain. At the same time, the surface low shifts to the south of the original westward track, which is primarily influenced by strong adiabatic warming associated with the downslope wind. The primary surface cyclone then resumes its original westward movement and symmetric circulation on the lee side once it moves away from the mountain. The deflection of the cyclone and low pressure centers at midlevels, such as $\sigma = 3$ km, are similar to those at the surface. Both vorticity and PV budgets are calculated to help understand the contributions from individual terms at different stages when a cyclone drifts over an idealized topography.

1. Introduction

When a tropical cyclone passes over a mountain range, its track, circulation, translation speed, strength, and precipitation are significantly influenced by the topography and propose a challenging problem for weather forecasters. One well-known example is the impact of the Central Mountain Range (CMR) of Taiwan on impinging typhoons. The CMR, whose dominant peak has a height of 3997 m above mean sea level, runs through Taiwan in a north-northeast–south-southwest direction with a width of about 120 km, a length of about 300 km, and an average height of 2 km (Fig. 1). Since Taiwan is surrounded by oceans, it provides a unique environment for studying the orographic effects on propagating tropical cyclones. Similar problems also occur in other parts of the world, such as those in the northern Philippines (Brand and Blelloch 1973; Kintanar and Amadore 1974) and in the Caribbean Islands (Hebert 1980).

According to extensive observational studies by Wang (1980, 1989), when a typhoon impinges on Taiwan's CMR from east at a certain angle, its track may remain continuous or become discontinuous (Fig. 2). For continuous track typhoons, the typhoon may (a) simply continue its path over the mountain range; (b) deflect, and remain for some time on the eastern side of the CMR before passing over the mountain; or (c) have its upper-level center propagate over the mountain range while its low-level center is deflected southward and fills. For discontinuous track typhoons, two or three secondary lows tend to form on the downstream side of the CMR, one of which then develops and replaces the center of the parent typhoon. Thus, the typhoon appears to jump over the mountain range. Based on these observations, Wang (1980) proposed that the typhoon is steered by the rear part of its own circulation and the basic flow when the front part of the circulation is blocked by the mountain range as the typhoon impinges

Corresponding author address: Dr. Yuh-Lang Lin, Department of Marine, Earth and Atmospheric Sciences, North Carolina State University, Raleigh, NC 27695-8208.
E-mail: yl_lin@ncsu.edu.

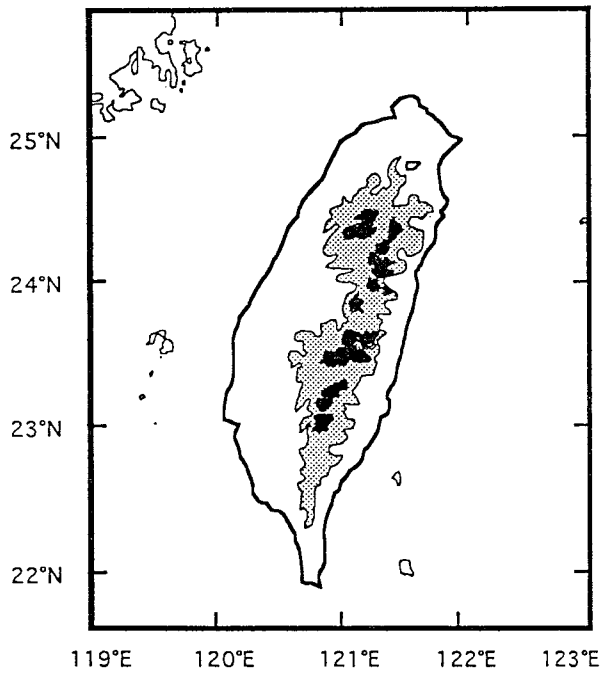

FIG. 1. Taiwan topography. The contour of 1 km is shaded and that of 3 km is darkened.

the CMR from east. Therefore, the typhoon center is deflected toward the north before and then toward south after passing over the CMR. However, this does not seem to be able to explain the southward deflection as is observed in some cases (Fig. 3a).

Using a primitive equation model, Chang (1982) found that the tropical cyclone's passage induces a mean cyclonic circulation around the mountain, which forces the cyclone to take a cyclonic track around the northern end of the mountain. As pointed out by Bender et al. (1987), the cyclone track in Chang's simulation may be influenced by the relatively coarse grid resolution (60 km). In addition, the idealized mountain used in Chang's study—that is, 240 km $\times$ 480 km—is much larger than the real Taiwan mountain, which may also influence the cyclone tracks. A northward deflection upstream for a westward propagating cyclone impinging on Taiwan's CMR has also been simulated by Bender et al. (1985, 1987). The northward deflection is explained by the deflection of environmental flow in Bender et al. (1987). A close inspection of their ocean control cases (without mountains; cases T10 and T5) does show a northward component far upstream, which tends to force the typhoon to land on the northeast coast of Taiwan. Thus, the typhoon would be deflected to the north by the northern branch of the upstream splitting flow. The northward deflection of tropical cyclones in ocean control cases was also evident in Yeh and Elsberry (1993a). In addition, like Chang (1982), Yeh and Elsberry also adopted a relatively larger mountain (320 km $\times$ 410 km) than Taiwan's CMR. Therefore, the orographic influence on tropical cyclone track needs further investigation.

Chang (1982) found that secondary vortex centers form in the lee trough, which may develop when they are in phase with the upper-level cyclone center. He proposed that the horizontal advection of positive vorticity in conjunction with leeside vorticity stretching results in a mean positive vorticity around the mountain. Chan (1984) also found a definite link in the local change of relative vorticity and tropical cyclone movement over a flat surface. On the other hand, Yeh and Elsberry (1993b) proposed that cyclone reorganization downstream of the mountain may occur as 1) a downward extension from the upper-level remnants of the typhoon or 2) an upward growth of a low-level secondary vortex. For a development mechanism of the second type, a new low-level center separates from the original cyclone (or the terrain-induced pressure trough) and becomes the center about which the tropical cyclone reorganizes itself. However, the relationship between these two types of vorticity development remains unclear.

Using a numerical shallow water model, Smith and Smith (1995) found that vortex interaction with idealized topography results in a pair of trailing banners of vorticity, which become wrapped up into the primary vortex as it drifts away. The potential vorticity (PV) production over the lee side when the cyclone approaches the mountain is explained by the transition from the irrotational flow regime to the regime of flow over a mountain with wakes through wave breaking. Results of tank experiments (e.g., Hwang et al. 1977; Brand et al. 1982) may be compared with those of shallow water simulations (e.g., Smith and Smith 1995) to help understand the basic dynamics of the formation of secondary vortices. However, a direct application of these results from both tank experiments and shallow water models to the real atmosphere is limited due to the underlying assumptions made in these experiments and models, such as a free upper surface and the lack of stratification. On the other hand, PV generation associated with regime transition may play an important role in modifying the track and circulation of a tropical cyclone when it passes over a mountain.

For low Froude number, nonrotating, uniform flow over a three-dimensional mountain, Schar and Durran (1997) found that the generation of leeside vorticity is produced by the vertical tilting of baroclinically generated horizontal vorticity upstream, as originally proposed by Smolarkiewicz and Rotunno (1989), during the early phase over a nondimensional time of $O(1)$. On the other hand, it is generated by PV, as originally proposed by Smith (1989a), during the later phase over nondimensional times of $O(10)$ and $O(100)$. In addition, Schar and Durran (1997) have identified two flow regimes: (a) flow splitting with wake for very low Froude number (e.g., Fr = 1/3) and (b) flow over with wave breaking for low Froude number (e.g., Fr = 1/1.5). A

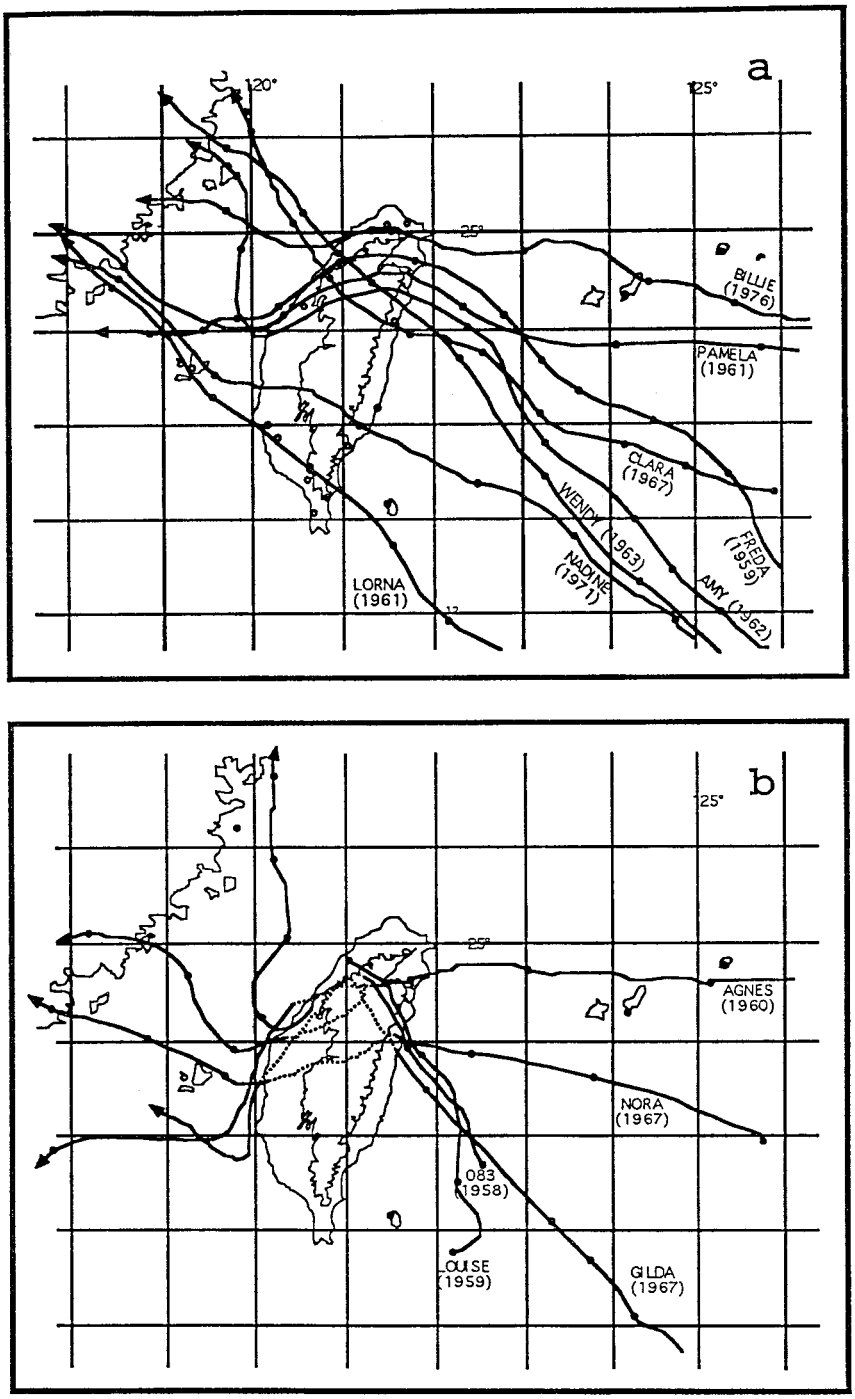

FIG. 2. Two types of typhoon tracks: (a) continuous and (b) discontinuous (after Wang 1980)

regime diagram of no wake, long straight wake, and steady wake eddies or eddy shedding has been proposed by Smith et al. (1997). A Bernoulli deficit develops either from weak dissipation throughout the elongated wake (regime a) or as the result of strong localized dissipation in the wave-breaking region (regime b). At a certain location upstream of the mountain, the local Froude number increases when a cyclone approaches the mountain because the local wind increases with time. Thus, a transition in flow regimes will occur and may generate PV. This deserves further investigation.

The flow circulations associated with typhoons near

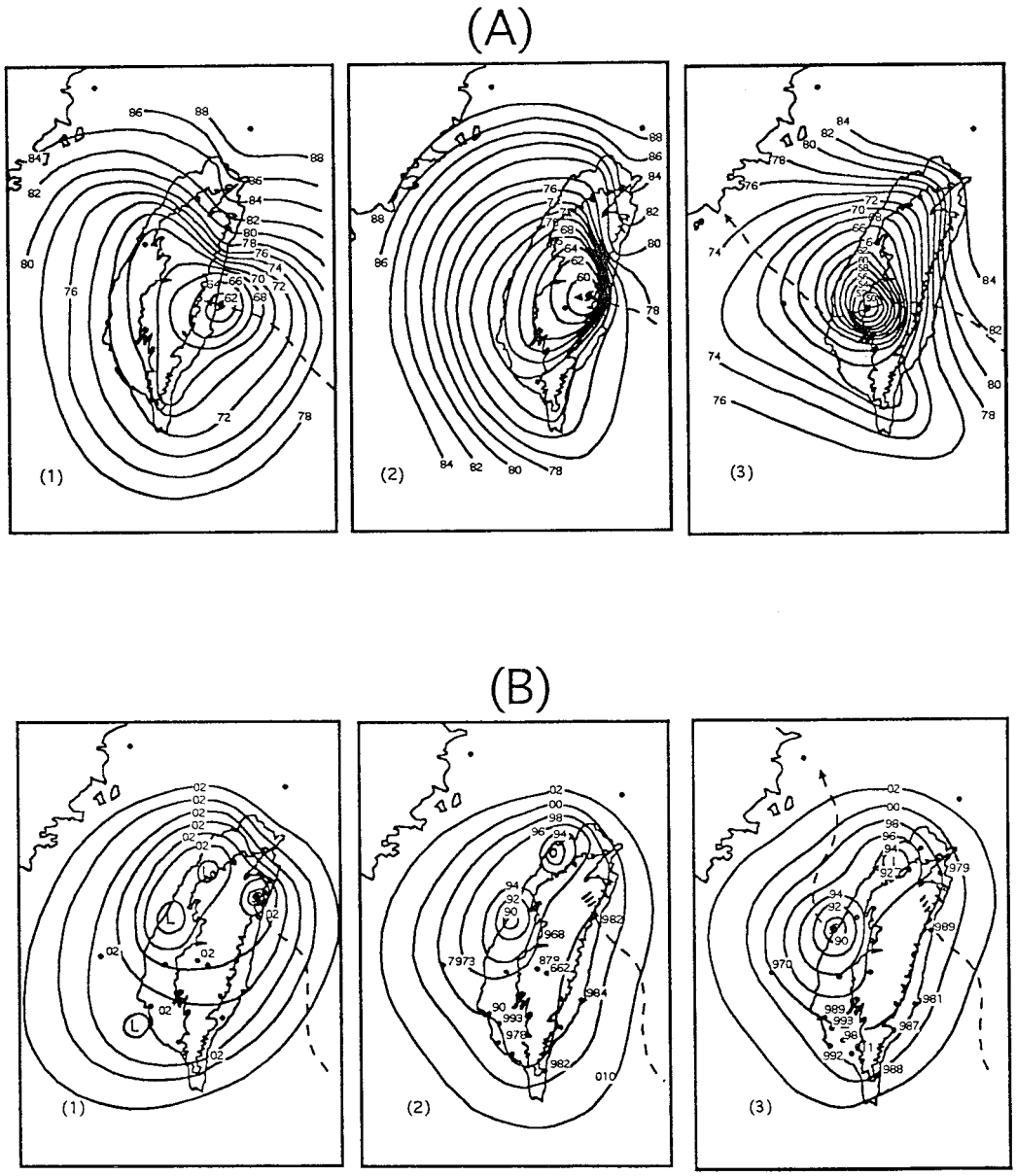

FIG. 3. Flow circulations associated with a typhoon that has (a) continuous track and (b) discontinuous track (after Wang 1980)

the CMR may become extremely complicated, due to the existence of upstream blocking, flow splitting, as well as the formation of downstream hydraulic jump and severe downslope wind. Based on observational analysis, Wang (1980) proposed that the circulation is only slightly modified by the mountain range for typhoons with a continuous track, whereas it is significantly modified for typhoons with a discontinuous track (Fig. 3b). These factors warrant further study.

In this study, we will adopt a primitive equation numerical model to investigate the orographic influence on a drifting cyclone over idealized topography similar to that of Taiwan's CMR. The cyclone is in gradient wind balance initially. The numerical model is briefly described in section 2. Two types of basic experiments—the mountain only case (cases M1–M3) and cyclone only case (case V)—will be also presented and discussed in this section, which will help to understand the dynamics of cyclone passing over mountains. In section 3, we will investigate the effects of an idealized topography on a drifting cyclone. Orographic influence on flow circulation, cyclone track, and flow regime transition and its relationship with PV generation will be studied. Conclusions and discussions are given in section 4.

2. The model and basic simulations

a. The model

The numerical model used in this study is based on the three-dimensional primitive equations for a stably stratified, Boussinesq fluid. The model equations are transformed to the terrain-following coordinate $\sigma = z_T(z - h)/(z_T - h)$, where $h(x, y)$ is the terrain elevation and z_T is the top of the computational domain (Gal-Chen and Somerville 1975). In the absence of moisture, the horizontal momentum equations, hydrostatic equation, incompressible continuity equation, and the thermodynamic equation, written in terms of the transformed vertical coordinate σ, are

$$\frac{\partial(Hu)}{\partial t} + \frac{\partial(Huu)}{\partial x} + \frac{\partial(Hvu)}{\partial y} + \frac{\partial(H\dot{\sigma}u)}{\partial \sigma} - f_0\tilde{v} = -\frac{1}{\rho_0}\left[\frac{\partial(H\tilde{p})}{\partial x} + \frac{\partial(G\tilde{p})}{\partial \sigma}\right] + \frac{\partial(-\overline{u'w'})}{\partial \sigma} \quad (1)$$

$$\frac{\partial(Hv)}{\partial t} + \frac{\partial(Huv)}{\partial x} + \frac{\partial(Hvv)}{\partial y} + \frac{\partial(H\dot{\sigma}v)}{\partial \sigma} - f_0\tilde{u}, = -\frac{1}{\rho_0}\left[\frac{\partial(H\tilde{p})}{\partial y} + \frac{\partial(J\tilde{p})}{\partial \sigma}\right] + \frac{\partial(-\overline{v'w'})}{\partial \sigma}, \quad (2)$$

$$\frac{1}{H}\frac{\partial \tilde{p}}{\partial \sigma} = \rho_0 g\frac{\tilde{\theta}}{\theta_0}, \quad (3)$$

$$\frac{\partial(Hu)}{\partial x} + \frac{\partial(Hv)}{\partial y} + \frac{\partial(H\dot{\sigma})}{\partial \sigma} = 0, \text{ and} \quad (4)$$

$$\frac{\partial(H\theta)}{\partial t} + \frac{\partial(Hu\theta)}{\partial x} + \frac{\partial(Hv\theta)}{\partial y} + \frac{\partial(H\dot{\sigma}\theta)}{\partial \sigma} = \frac{\partial(-\overline{\theta'w'})}{\partial \sigma}, \quad (5)$$

where

$$H = \left|\frac{\partial z}{\partial \sigma}\right| = 1 - \frac{h}{z_T}, \quad (6)$$

$$G = -\left(\frac{\partial z}{\partial x}\right)_\sigma = \left[\left(\frac{\sigma}{z_T}\right) - 1\right]\frac{\partial h}{\partial x}, \text{ and} \quad (7)$$

$$J = -\left(\frac{\partial z}{\partial y}\right)_\sigma = \left[\left(\frac{\sigma}{z_T}\right) - 1\right]\frac{\partial h}{\partial y}. \quad (8)$$

Here $\dot{\sigma}$ is related to the vertical velocity w by

$$\dot{\sigma} = \frac{1}{H}(w + Gu + Jv). \quad (9)$$

The symbols $\tilde{u}$, $\tilde{v}$, $\tilde{p}$, and $\tilde{\theta}$ represent deviations from the initial basic-state fields that are in geostrophic and hydrostatic balance. The turbulent fluxes are parameterized according to an eddy viscosity approximation:

$$\overline{u'w'} = -K_m\frac{\partial u}{\partial z} = -K_m\frac{1}{H}\frac{\partial u}{\partial \sigma}, \quad (10)$$

$$\overline{v'w'} = -K_m\frac{\partial v}{\partial z} = -K_m\frac{1}{H}\frac{\partial v}{\partial \sigma}, \text{ and} \quad (11)$$

$$\overline{\theta'w'} = -K_h\frac{\partial \theta}{\partial z} = -K_m\frac{1}{H}\frac{\partial \theta}{\partial \sigma}. \quad (12)$$

Based on dimensional arguments, the eddy exchange coefficients for momentum and heat are given by

$$K_m = c_0 l_k e^{1/2} \quad \text{and} \quad K_h = \alpha_h K_m, \quad (13)$$

respectively, where e, defined as $e = 0.5(\overline{u'^2} + \overline{v'^2} + \overline{w'^2})$, is the turbulent kinetic energy (TKE), l_k the turbulent mixing length scale, c_0 a numerical constant, and α_h the reciprocal of the turbulent Prandtl number for potential temperature θ. TKE is predicted to obtain K_m. This procedure is, so-called, one and one-half–order turbulence or TKE closure. The TKE equation can be written as

$$\frac{\partial e}{\partial t} + u\frac{\partial e}{\partial x} + v\frac{\partial e}{\partial y} + w\frac{\partial e}{\partial z} = -\overline{u'w'}\frac{\partial u}{\partial z} - \overline{v'w'}\frac{\partial v}{\partial z} + \frac{g}{\theta_0}\overline{w'\theta'} - \frac{\partial}{\partial z}\left(\overline{w'e'} + \frac{1}{\rho_0}\overline{p'w'}\right) - \epsilon. \quad (14)$$

The energy dissipation rate ε and the diffusion terms in Eq. (14) are parameterized as follows:

$$\epsilon = c_1 e^{3/2}/l_\epsilon \quad (15)$$

and

$$-\frac{\partial}{\partial z}\left(\overline{w'e'} + \frac{1}{\rho_0}\overline{p'w'}\right) = K_e\frac{\partial e}{\partial z}, \quad (16)$$

where c_1 is a numerical constant, l_ε the turbulent dissipation length scale, and K_e the eddy exchange coefficient for TKE. Here K_e is related to K_m through

$$K_e = \alpha_e K_m, \quad (17)$$

where α_e is the reciprocal of the turbulent Prandtl number for TKE. The TKE closure model suffers from the difficulty of the proper specification of the turbulence length scale. There exist many formulations for the length scale in the literature (e.g., Lacser and Arya 1986). In this study, we use the length scale formulation developed by Bougeault and Lacarrere (1989). The length scale for turbulent eddies in their formulation is primarily determined by the resistance to vertical displacements due to the static stability. The empirical constants used in this study are therefore $(c_0, c_1, \alpha_h, \alpha_e) = (0.4, 0.714, 1.0, 1.0)$.

The model has the following characteristics:

- The time-dependent governing equations are solved on an Arakawa-C staggered grid (e.g., Haltiner and Williams 1980).

TABLE 1. Summary of parameters used in numerical experiments. Other parameters: $h_0 = 2.5$ km, $a = 40$ km, and $b = 120$ km. The initial cyclone location is at $(x/a, y/a) = (12.5, 0)$.

Case	(U, V) (m s^{-1})	Fr	$\hat{h}$	f_o (s^{-1})	r_{max} (km)	Characteristics of exp.
M1	$(-10, 0)$	0.4	2.5	5.8×10^{-5}	NA	Mountain only, very low Froude number, $f_o \neq 0$
M2	$(-10, 0)$	0.4	2.5	0	NA	Same as M1 except $f_o = 0$
M3	$(-10, 0)$	0.8	1.25	5.8×10^{-5}	NA	Same as M1 except larger Fr
V	$(-10, 0)$	0.4	2.5	5.8×10^{-5}	180	Cyclone only
MV	$(-10, 0)$	0.4	2.5	5.8×10^{-5}	180	Cyclone moves from east over a mountain

The vertical profile of v_{max} is given by

v_{max} (m s^{-1})	z (km)
20	0–4.5
15	5
10	6
0	7
−5	8
−10	9
−5	10
0	11–15

- The third-order Adams–Bashforth scheme is used for time marching.
- The horizontal (vertical) advection terms are approximated using quadratic conservative fourth- (second-) order-centered finite differences.
- A free-slip lower-boundary condition is used.
- A radiation upper-boundary condition (Klemp and Durran 1983) is used.
- The Orlanski (1976) radiation condition consistent with the third-order Adams–Bashforth time differencing is applied for all prognostic variables except TKE along the lateral boundaries. A zero-gradient lateral boundary condition is used for TKE.
- The horizontal domain averages are subtracted from perturbation pressure fields in every grid point at every time step, which not only reduces truncation errors caused by the topographic terms but also prevents unrealistic pressure perturbation field (Clark 1977).
- A five-point numerical smoother or diffusion (Shapiro 1970) is applied at every time step in both the horizontal and vertical directions.

Details of numerical formulation of the model can be found in Han (1998). This version of the model has been tested rigorously against Smith's (1980) linear theory for high Froude number uniform flow past a circular mountain and the numerical results of Smolarkiewicz and Rotunno (1989), Olafsson and Bougeault (1996), and Schar and Durran (1997).

A uniform, stably stratified basic flow is introduced instantaneously at $Ut/a = 0$. The Brunt–Väisälä frequency associated with this initial flow is taken to be 0.01 s^{-1} for all experiments discussed in this study. An f-plane approximation has been made. The Coriolis parameter f_0 is taken to be 5.8×10^{-5} s^{-1}. The flow is inviscid throughout the entire model domain. The vertical grid interval is 500 m, whereas the horizontal grid interval in both x and y directions is 20 km. Thus, the grid numbers in x, y, and z directions are $101 \times 81 \times 31$ for the domain size of 2000 km $\times$ 1600 km $\times$ 15 km, respectively. The idealized bell-shaped topography is prescribed as

$$h(x, y) = \frac{h_0}{\left(\frac{x^2}{a^2} + \frac{y^2}{b^2} + 1\right)^{3/2}}, \tag{18}$$

where h_0 is the mountain height, and a and b the mountain half-widths in the x and y directions, respectively. In this study, we have adopted values that adequately represent Taiwan's CMR, $h_0 = 2.5$ km, $a = 40$ km, and $b = 120$ km. Note that the whole scale of the mountain is roughly equal to four times of the half-width.

The cyclone embedded in the easterly flow is initialized with a prescribed tangential velocity following Chang (1982),

$$v_\theta(r) = v_{max} \frac{r}{r_{max}} \exp\left\{\frac{1}{2}\left[1 - \left(\frac{r}{r_{max}}\right)^2\right]\right\}, \tag{19}$$

where v_{max} is the maximum tangential velocity at a radius of r_{max} from the cyclone center. The vertical profiles of v_{max} and the values of r_{max} for cases performed in this study are given in Table 1. A nonlinear, nondivergent initialization method is used to obtain the velocity, pressure, and potential temperature fields for the cyclone. The final balanced velocity field is in gradient wind balance and nondivergent, which will differ slightly from Eq. (19). The details of the initialization procedure can be found in appendix A.

b. Basic simulations

Before investigating the orographic influence on propagating vortices, we will discuss two types of basic

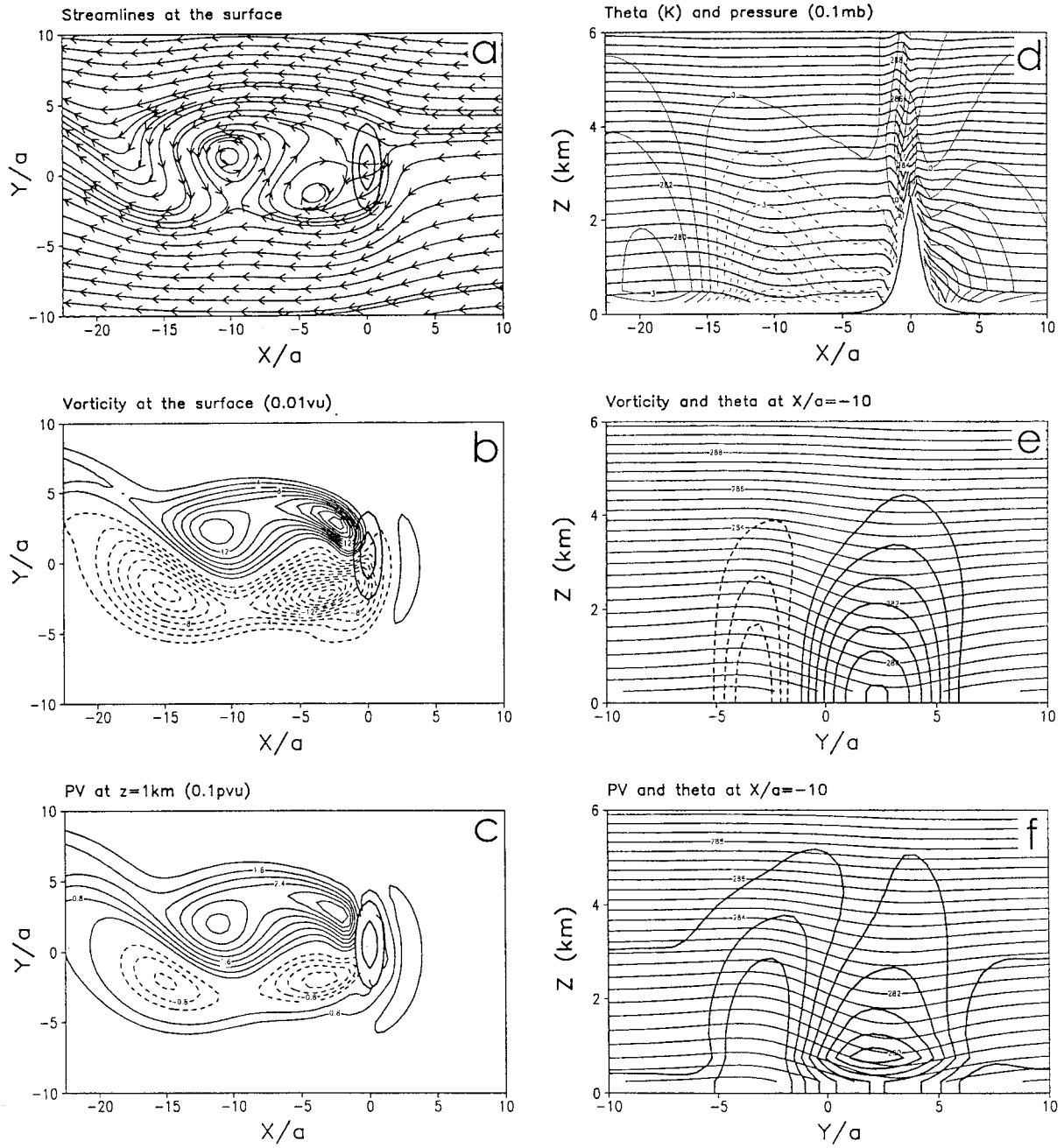

FIG. 4. Case M1: (a) surface streamlines, (b) surface vertical vorticity, (c) PV at $z = 1$ km, (d) vertical cross section of potential temperature and p at $y/a = 0$, (e) vertical vorticity and potential temperature at $x/a = -10$, and (f) PV and potential temperature at $x/a = -10$ for an easterly flow over an idealized topography without cyclone after $Ut/a = 40$. Fr $= 0.4$ and $f_0 = 5.8 \times 10^{-5}$ s^{-1}. The other flow and mountain parameters are summarized in Table 1. The $2h/3$ and $h/3$ mountain height contours are denoted. Positive (negative) vorticity and PV are denoted by solid (dashed) curves. The x and y scales are nondimensionalized by the mountain half-width in the x direction, a.

experiments: one with mountain only (cases M1–M3), and the other with cyclone only (case V). In this study, we will limit our discussions on basic dynamics and rotational effects.

Figure 4 shows the surface streamlines, surface vertical vorticity, and potential vorticity at $z = 1$ km, and vertical cross sections of θ and perturbation pressure, vorticity, and PV fields for a uniform adiabatic, continuously stratified flow over the idealized topography [Eq. (18)] after the nondimensional time $Ut/a = 40$ (case

M1). The basic flow, mountain, and initial cyclone parameters are summarized in Table 1. The vertical vorticity is calculated at the surface. The streamline and cross section θ fields indicate that a significant portion of the low-level flow is blocked by the mountain and a low nonrotating Froude number (Fr $= U/Nh_0 = 0.4$) and a large aspect ratio ($h_0/a \sim 2.5$ km/40 km $= 0.0625$) flow. A significant portion of the upstream (i.e., eastern slope) fluid particles flow southward since the weakened easterly wind is out of balance geostrophically. Over the mountain peak, the hydrostatic mountain wave is very weak because most of the flow is blocked by the high mountain and is deflected to the north and south, instead of climbing up and passing over the mountain. Downstream of the mountain, a pair of cyclonic and anticyclonic vortices are also generated by the flow, similar to that simulated by Sun et al. (1991) and Lin et al. (1992) for rotating flow over Taiwan's CMR. These vortices keep shedding downstream and new ones keep forming along the immediate lee slope of the mountain. The cyclonic vortex may be regarded as a mesoscale cyclone, since it has a closed circulation and is collocated with a low pressure center, as found by Lin et al. (1992). Crook et al. (1990) has also simulated the Denver cyclone in a nonrotating fluid system. The high-low pressure couplet across the mountain range (Fig. 4d) is hydrostatically produced from the mesoscale flow over the mountain, which is consistent with existing mountain wave theories (e.g., Smith 1979).

The vertical vorticity field shows that positive and negative vorticity are produced in the north and south of the mountain on the lee side, respectively. The symmetry of positive and negative vorticities simulated in a nonrotating flow (e.g., Smolarkiewicz and Rotunno 1989) is destroyed by the Coriolis force. The pattern of potential vorticity field is very similar to that of vertical vorticity field (Figs. 4b and 4c).

From the streamline and vorticity fields (Figs. 4a and 4b) and the vertical cross section of θ field (Fig. 4d), the flow appears to fall into the regime of flow splitting. It will be discussed later that the regime transition from splitting-dominated flow to wave-breaking dominated flow tends to generate new PV through turbulent mixing and numerical diffusion, which can play a role similar to friction in the real atmosphere. The vorticity and PV banners extend far downstream. In addition, areas of weak positive and negative vorticity are also generated upstream of the mountain near the surface (Fig. 4b). A region of weak positive PV is also generated upstream (Fig. 4c). These regions of weak upstream vorticity and PV are absent in a nonrotating flow (Fig. 5c). The generation of lee vortices in an inviscid, nonrotating flow was first simulated by Smolarkiewicz and Rotunno (1989). They proposed that the leeside vorticity is produced by the vertical tilting of baroclinically generated horizontal vorticity. On the other hand, Smith (1989a) proposed that the leeside vorticity can be produced by PV generation. Using a numerical model, Schar and Durran (1997) found that the leeside vertical vorticity is generated by the tilting of horizontal vorticity during the early phase over a nondimensional time of $O(1)$, in which the flow is essentially inviscid and adiabatic and PV is conserved. However, they also found that the flow is controlled by dissipation and is accompanied by the PV generation at the later phase over a nondimensional time of $O(10)$ to $O(100)$. In the absence of Coriolis force, the flow pattern (Fig. 5) is symmetric with respect to $y/a = 0$ and is similar to earlier simulations (e.g., Smolarkiewicz and Rotunno 1989; Schar and Durran 1997). The PV budget analysis at $Ut/a = 40$ (Fig. 17) indicates that the local rate of change of PV is contributed mainly by mixing and diffusion, which is consistent with Smith's PV generation mechanism and Schar and Durran's numerical results at the later phase.

Figure 6 shows a case similar to case M1 except with Fr $= 0.8$ (case M3), which gives a nondimensional mountain height ($\hat{h}$ or Fr^{-1}) of 1.25. The streamline field (Fig. 6a) indicates that most of the fluid parcels diverge when they climb up the mountain, and then converge on the lee side. The gravity waves overturn and break over the lee slope (Fig. 6d). Similar to the wake observed downstream of St. Vincent (Smith et al. 1997) and numerical simulations of the idealized flow with $\hat{h} = Nh_0/U = 1.5$ [Fig. 14a of Schar and Durran (1997)], a pair of positive and negative vorticity and PV banners are generated on the lee slope (Fig. 5). As mentioned earlier, the asymmetry is due to the rotational effect. Similar to that found in Schar and Durran (1997), the vorticity maximum and minimum are located at the surface (Fig. 6e), whereas those of PV are located above the surface—that is, 0.7 km in this case. The vertical cross section of potential temperature field (Fig. 6d) shows a region of strong wave breaking over the lee slope, which is responsible for generating the PV anomalies (Smith 1989a,c; Schar and Smith 1993a,b, Schar and Durran 1997). Obviously, this case falls into the regime of flow over the mountain with wave breaking. Unlike Schar and Durran (1997), but similar to Smith et al. (1997), the downstream extension of vorticity may be more appropriately called a wake, compared with that in case M1. The wave breaking is evidenced by the isentropes and the generation of TKE (Fig. 6d). The importance of investigating this case, as will be discussed later in more detail, is that at a certain location upstream of the mountain, the local Froude number increases when a cyclone approaches the mountain. This will induce a transition from the regime dominated by flow splitting to the regime dominated by wave breaking.

Figure 7 shows the pressure perturbation, vector wind, vertical vorticity, and PV fields at the surface for a cyclone defined by Eq. (19), which propagates in an easterly flow over a flat surface for $Ut/a = 10$–18 (case V). It appears that the cyclone is able to maintain its strength and integrity under the gradient wind balance when it propagates downstream with the basic flow. The

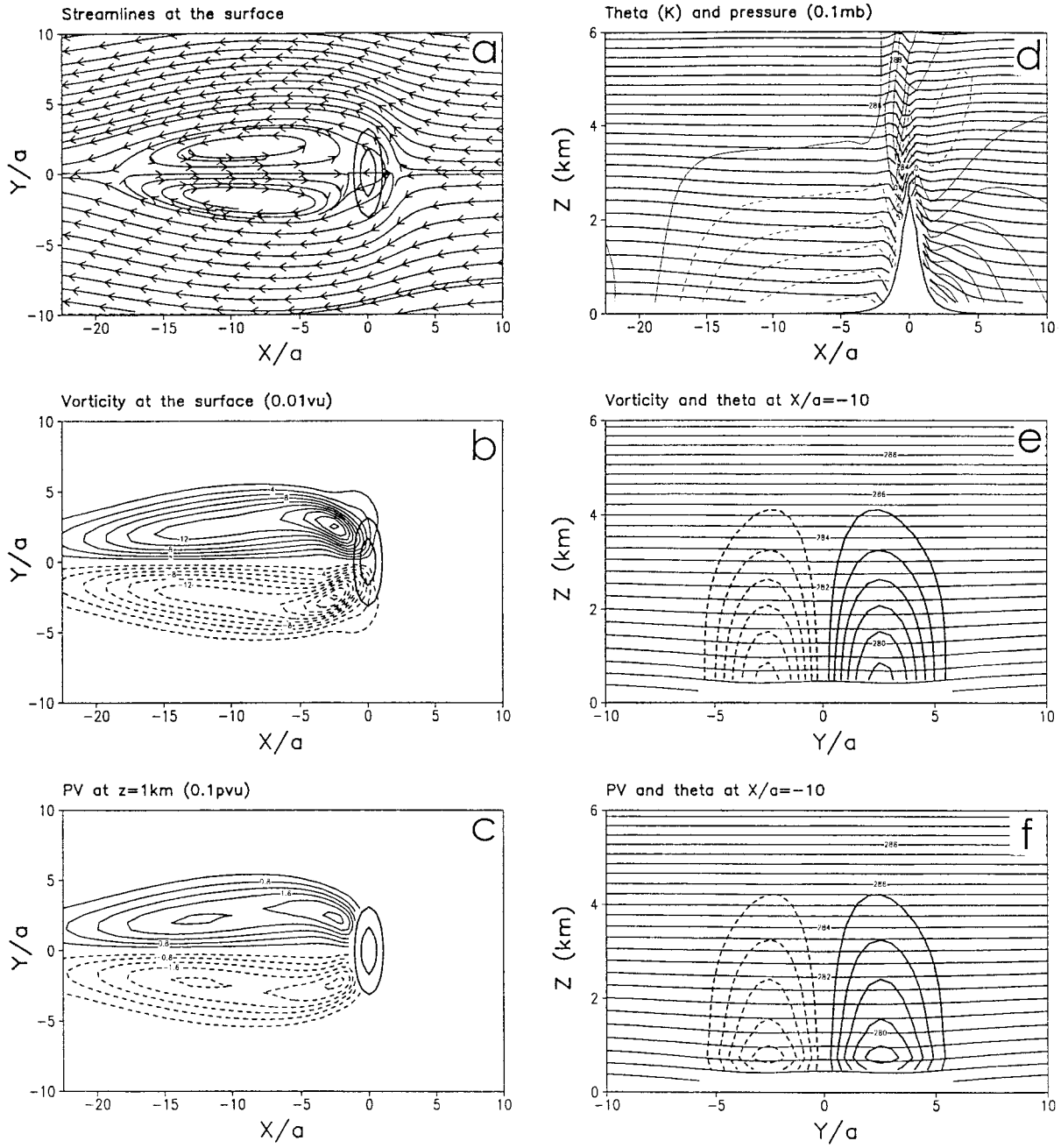

FIG. 5. Case M2: same as Fig. 4 except with no Coriolis force.

propagation speed is about the same as the basic wind (10 m s^{-1}). The vorticity and PV fields at the surface are almost symmetric for the entire integration period. Figure 8 shows time evolutions of maximum u, and minimum perturbation pressure, maximum vorticity, and maximum PV at the surface over the whole domain for case V. The maximum u, minimum perturbation pressure and vorticity (Figs. 8a–8c) decrease slightly with time due to numerical diffusion. The PV drops from 0.6 to 0.5 PV unit at $Ut/a \leq 2$, increases to 0.55 at $UT/a = 4$, and then decreases slightly to 0.45 PV unit at $Ut/a = 25$.

Figures 9a and 9b show the vertical cross sections of pressure perturbation, and vertical potential temperature fields at the cyclone injection time ($Ut/a = 0$), respectively. The gradient wind balance of the cyclone requires a strong low pressure region in the lower layer and a weak compensating high pressure in the upper layer.

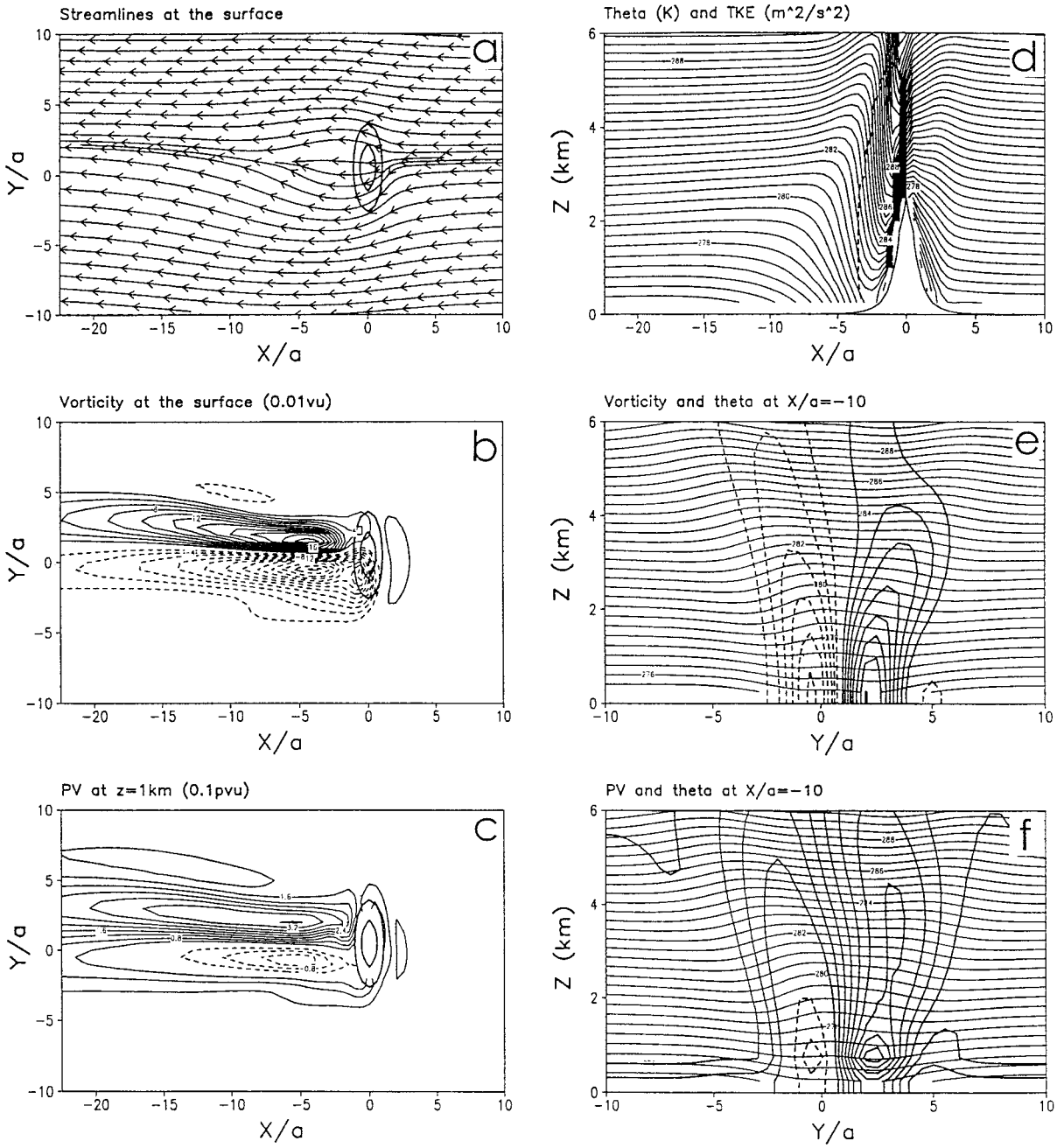

FIG. 6. Case M3: same as Fig. 4 except with Fr = 0.8. The bold dashed curve in (d) denotes the contour of TKE = 0.01 $m^2 s^{-2}$.

This gives a strong warm region in the lower layer and a weak compensating cold region in the upper layer, as required by the hydrostatic balance. Figures 9c and 9d show the same fields as those in Figs. 9a and 9b except at $Ut/a = 25$. The pressure perturbation field is maintained very well, while the strong vertical gradient of potential temperature smoothes out gradually with time. This adjustment gives the weakening of maximum u, and vorticity fields, and the oscillation in earlier times and weakening of the maximum PV at later times (as shown in Fig. 8).

3. Influence of idealized topography on a drifting cyclone

Figure 10 shows the streamline fields for a cyclone embedded in an easterly flow over an idealized, north–south-oriented mountain (case MV) at $Ut/a = 0$, 10,

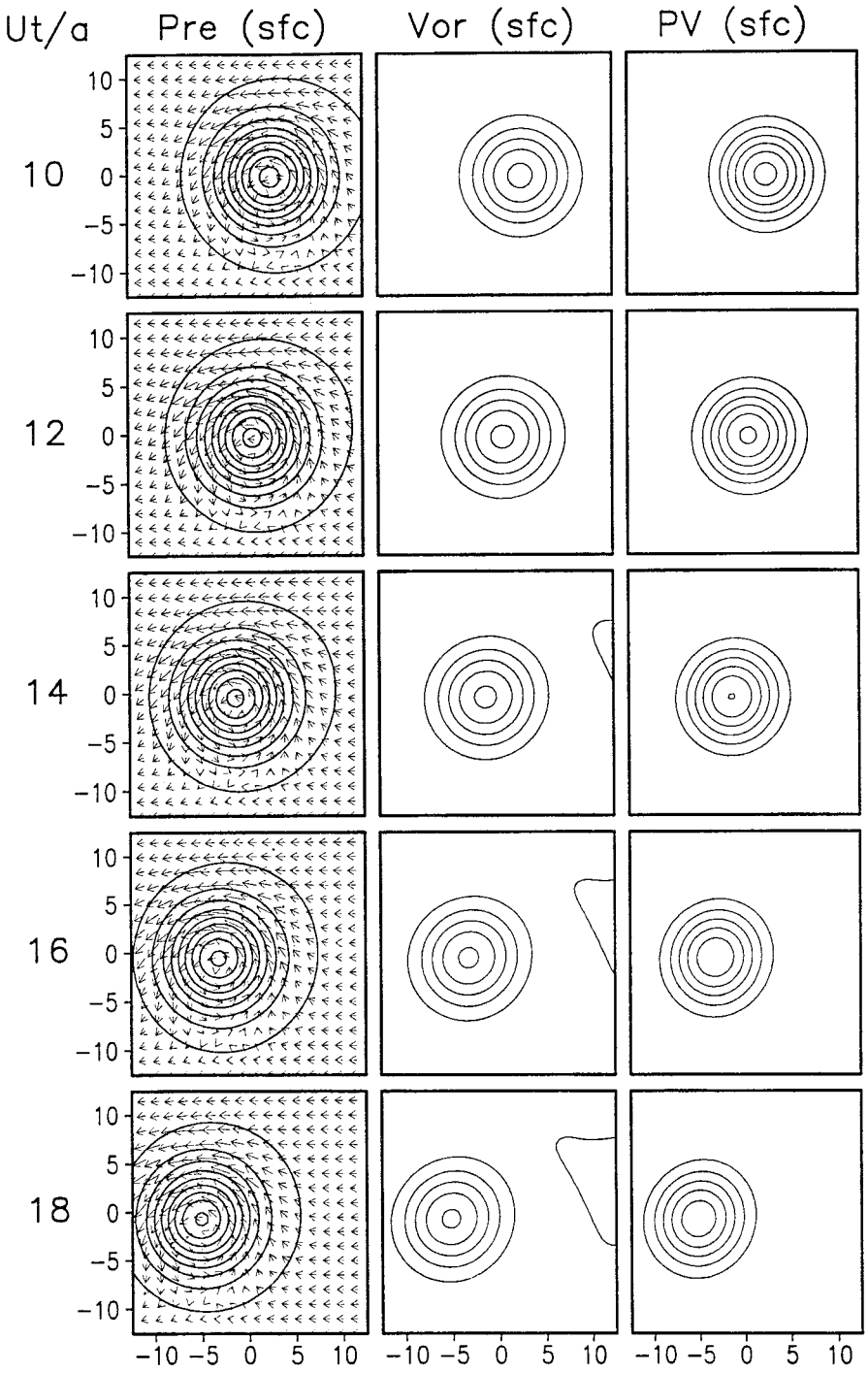

FIG. 7. Case V: Perturbation pressure (column 1), vertical vorticity and PV fields (columns 2 and 3) at the surface for a cyclone embedded in an easterly flow over a flat surface. Times shown are $Ut/a = 10$ to 18 with a time interval of 2, as indicated to the left side of the figure. Only the central portion of domain is shown. See Table 1 for flow, cyclone, and mountain parameters.

14, 16, 18, and 25. The flow parameters of the flow and mountain geometry are given in Table 1. The cyclone is injected into a uniform flow (10 m s^{-1}) over the mountain after a nondimensional time of 40, which is in gradient wind balance. Thus, the flow field over the mountain is well established before the cyclone is injected, which has a streamline field identical to Fig. 4a except with a cyclone located far upstream in this case.

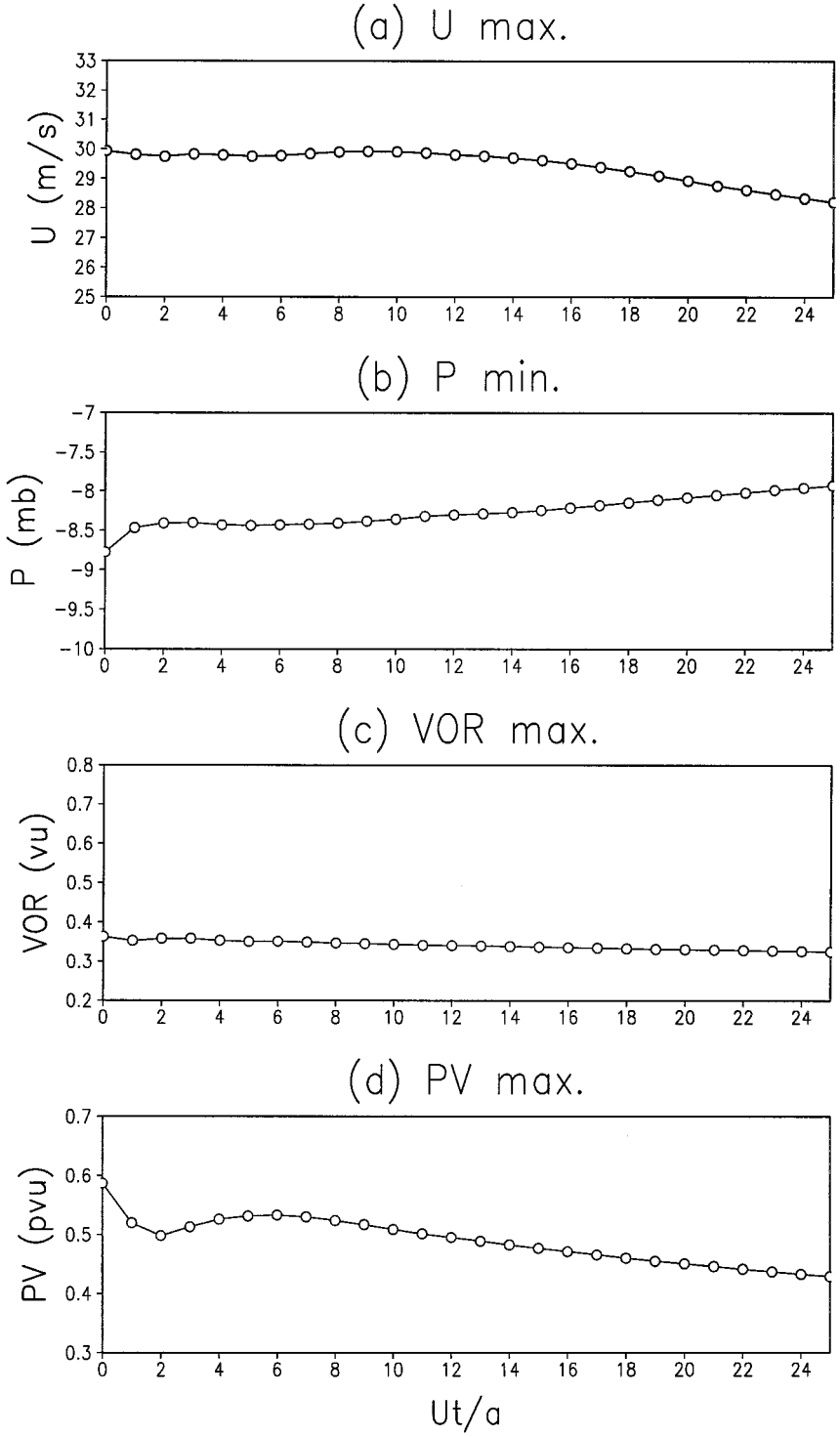

FIG. 8. Time evolution of (a) maximum surface *u*, (b) minimum surface *p*, (c) maximum vertical vorticity, and (d) PV at the surface for case V.

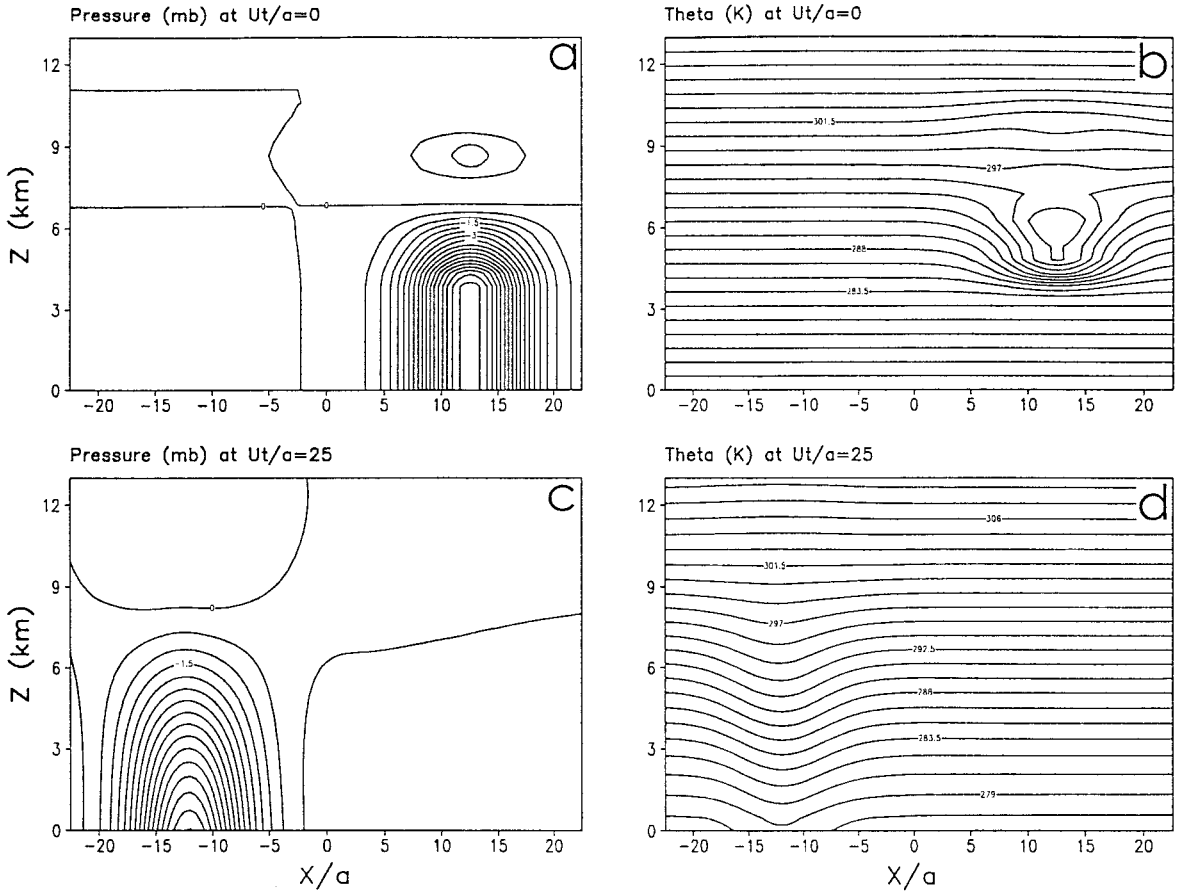

FIG. 9. Vertical cross sections of (a) p and (b) θ at $Ut/a = 0$. Panels (c) and (d): the same as (a) and (b) except at $Ut/a = 25$.

The primary cyclone starts to turn slightly south of the center line (i.e., $y/a = 0$) when it approaches the mountain, such as $Ut/a = 10$ (Fig. 10b). *A strong northerly jet is produced at the surface in between the mountain range and the primary cyclone due to blocking and channeling effects.* At the surface, most of the flow is blocked and forced to go around the mountain (Fig. 10b and 11), and the air parcels at higher levels are able to go over the mountain (Fig. 12c). Obviously, the flow at this time falls into the regime dominated by flow splitting. The pair of lee vortices keep shedding downstream, although the anticyclonic vortex tends to slow down the downstream propagation of the primary cyclone, as compared to the case with no preexisting lee vortices (not shown). At this time ($Ut/a = 10$), more air parcels are able to pass over the mountain compared to that at $Ut/a = 0$, because the local Froude number just upstream of the mountain increases as the cyclone approaches closer to the mountain. There exist two positive vorticity maxima, one is located upstream of the mountain, and the other is located in the southwest slope of the mountain peak (Fig. 11). *The positive vorticity associated with the primary cyclone appears to be blocked by the mountain* (Fig. 12a). The leeside positive vorticity is associated with a positive PV (Fig. 11). It will be shown later, along with the discussion of Figs. 18 and 19, that at this stage the leeside PV is generated by wave breaking through mixing and diffusion. A region of negative vorticity is present over the southern slope of the mountain, which is generated by column stretching (Fig. 18), as will be discussed later. The surface primary cyclone is still collocated with the primary low. The primary low remains roughly symmetric. *Two pressure ridges, one located over the northern upslope and the other over the southwest slope, and one trough, located on the lee side of the mountain, can be detected from the pressure fields* ($Ut/a = 10$ of Fig. 11). The low pressure region becomes elongated on the lee side, due to the adiabatic warming associated with the strong downslope wind. These pressure ridges have also been observed for typhoons passing over Taiwan's CMR (Wang 1980) and can be explained by hydrostatic response of flow over mountains.

At later times, such as $Ut/a = 14$ and 16, the original lee vortices keep shedding downstream, but are weakening (Figs. 10c and 10d). Two circulation centers associated with the primary cyclone coexist on both upslope and downslope. At $Ut/a = 18$, the original lee

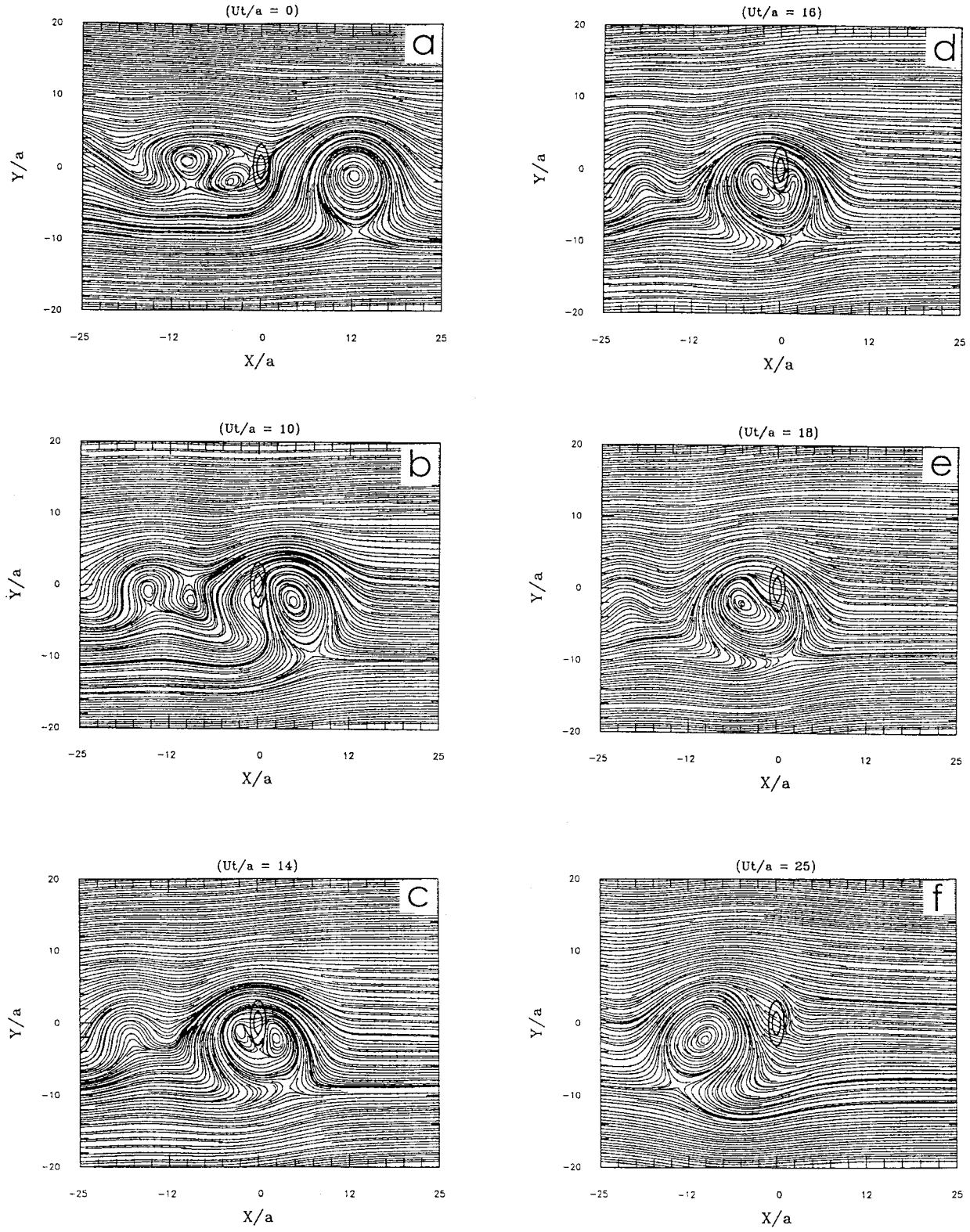

FIG. 10. Case MV: Streamline fields for case MV at $Ut/a = 0$, 10, 14, 16, 18, and 25 after cyclone injection. Note the cyclone is injected after the easterly uniform flow over the mountain for a nondimensional time of 40.

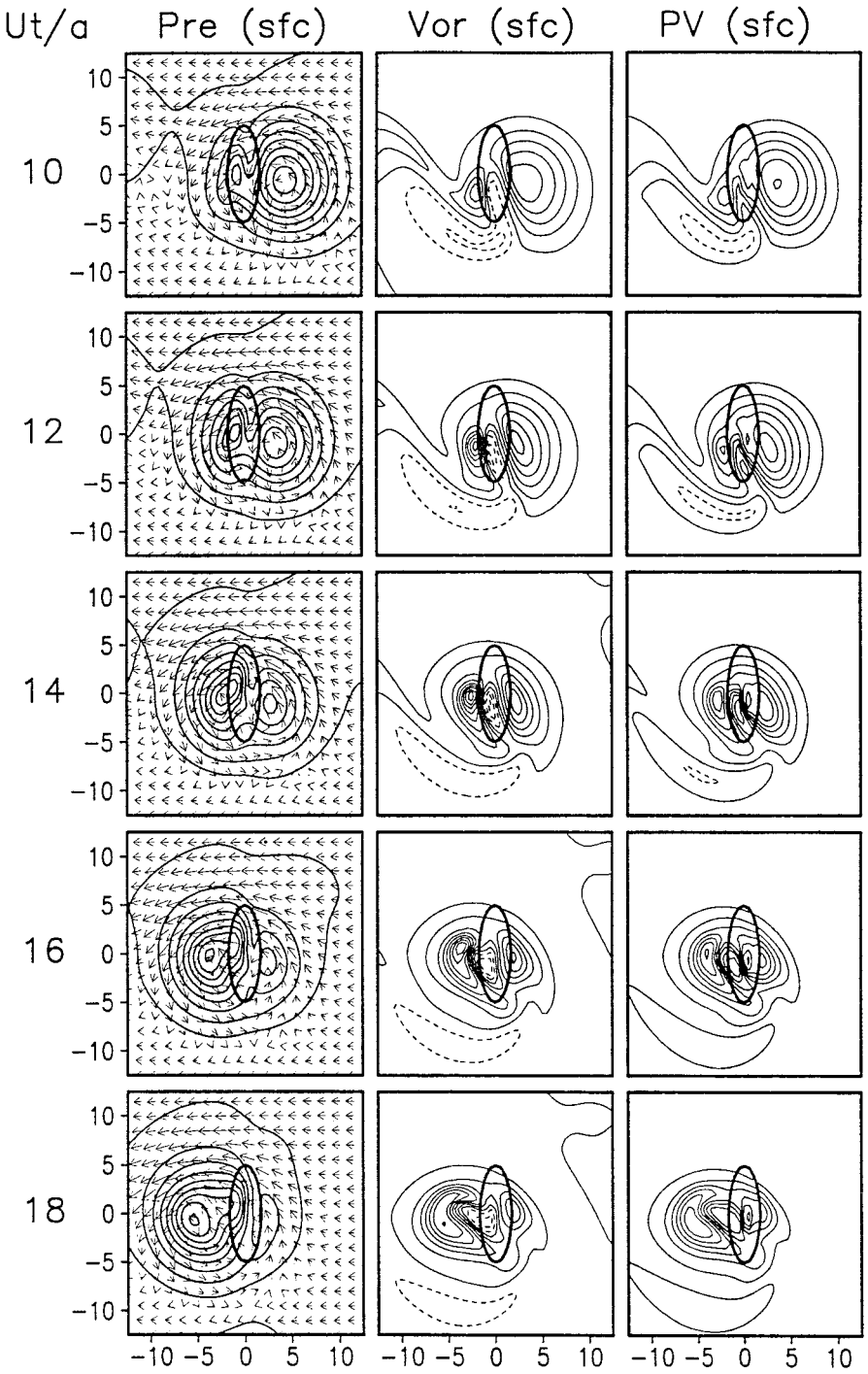

FIG. 11. Same as Fig. 7 except for a propagating cyclone embedded in an easterly flow over an idealized mountain range.

vortices become very weak and propagate out of the left boundary. The flow circulation is dominated by the primary cyclone, which is completely located on the lee side. The primary cyclone keeps propagating downstream and resumes its symmetric circulation as time proceeds (Fig. 10f).

The low over the lee side elongates in the north–south direction at $Ut/a = 12$ and 14 (Fig. 11). Two low centers exist simultaneously. One is located over the eastern slope, and the other is located over the western slope. The low on the western slope becomes stronger, which is produced by adiabatic warming associated with the

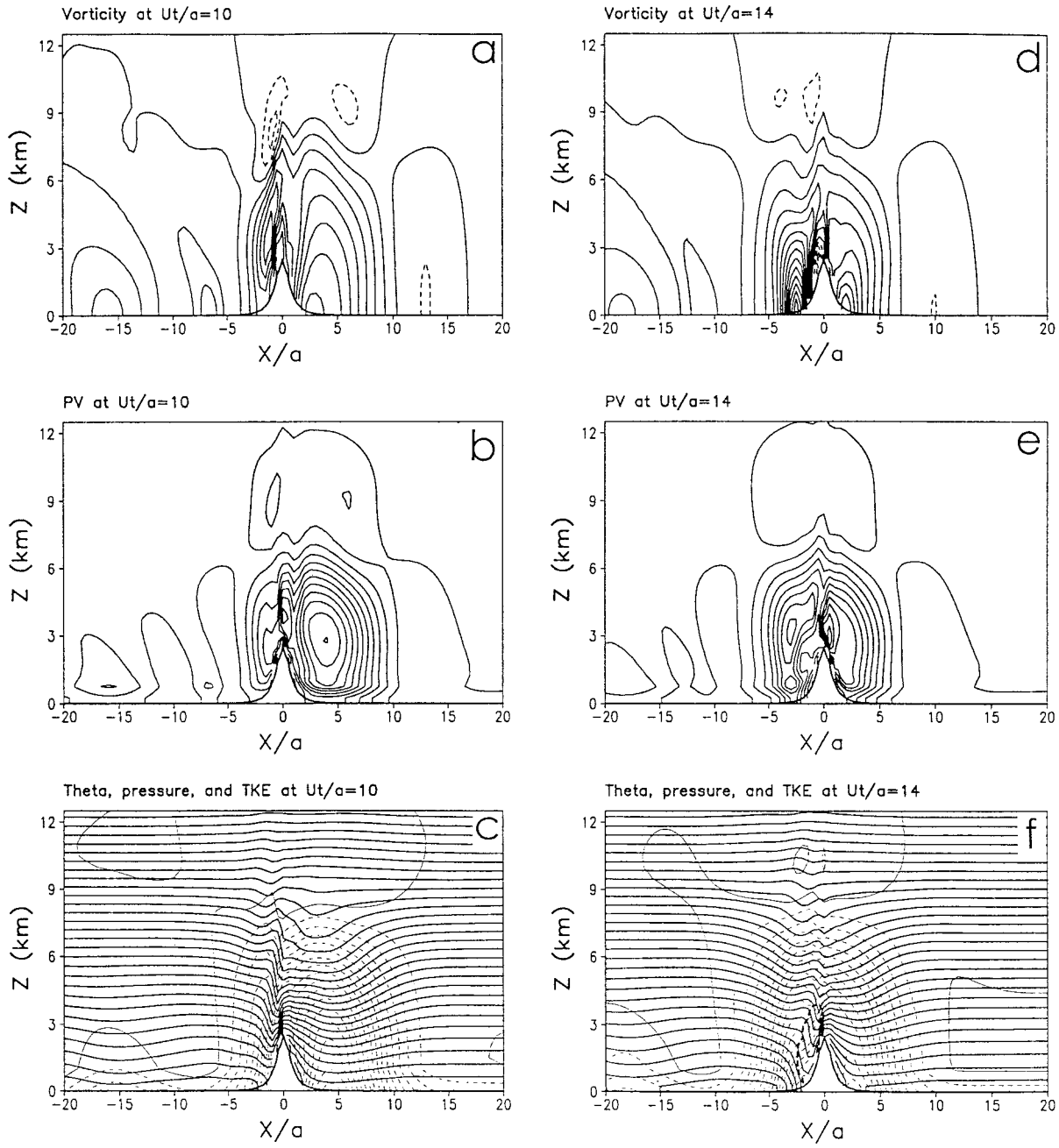

FIG. 12. Vertical cross sections of (a) vertical vorticity, (b) PV, and (c) pressure perturbation and potential temperature along $y/a = 0$ for case MV at $Ut/a = 10$. Panels (d)–(f): the corresponding fields at $Ut/a = 14$. The bold dashed curve on (f) is the TKE contour of 0.01 $m^2 s^{-2}$.

downslope wind, and is often referred to as a *secondary low* (e.g., Wang 1980). The inverted pressure ridge over the northeastern slope is produced by hydrostatic response of flow over mountains (Fig. 12f), which is consistent with mountain wave theory (e.g., Smith 1979) and resembles the pressure pattern observed in the vicinity of Taiwan's CMR (Fig. 3; Wang 1980). During this stage, the leeside vorticity strengthens dramatically and develops within a very small area. Although the primary cyclone has already passed over the mountain peak to the western slope, a significant portion of the vorticity and PV is still blocked upstream by the mountain (Fig. 12d). The vertical cross section of $y/a = 0$ also shows that there exists wave breaking over the lee slope, as evidenced by the isentropes as well as the significant increase of TKE, which is generated by tur-

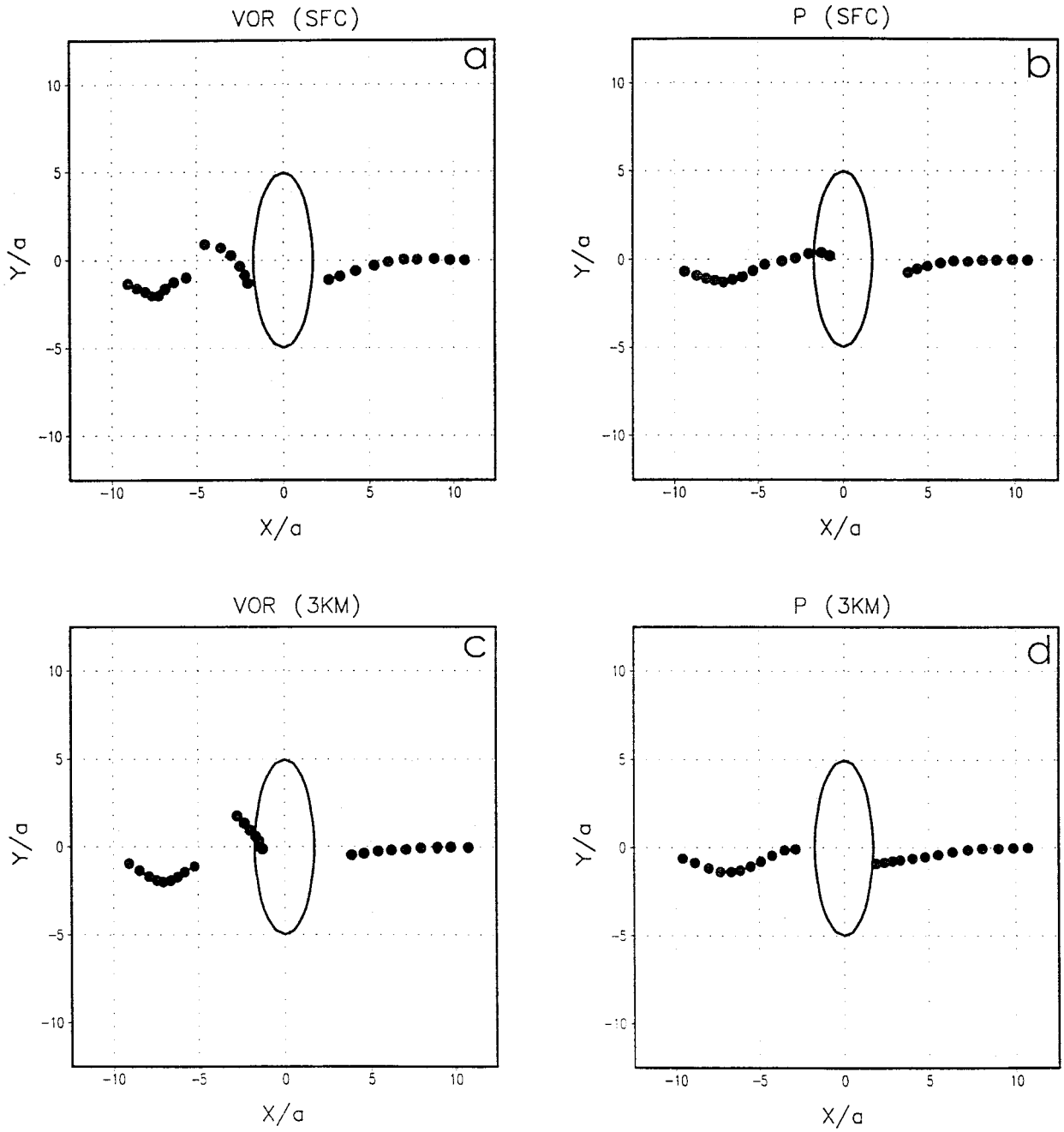

FIG. 13. Tracks of (a) surface vertical vorticity center, (b) surface low, (c) vertical vorticity center at $\sigma = 3$ km, and (d) low at $\sigma = 3$ km from $Ut/a = 2$ to 25 for case MV.

bulent mixing (Fig. 12f). The wave breaking is associated with the severe downslope wind and internal hydraulic jump.

The primary cyclone appears to decelerate and move farther southward at $Ut/a = 12$, accelerates over the southwestern slope at $Ut/a = 14$, and then moves northwestward to its original latitude until $Ut/a = 17$ (Figs. 11 and 13). After $Ut/a = 17$, the surface vorticity center moves farther southward and then westward. *This southward movement of the primary cyclone upstream of the mountain at $Ut/a = 12$ appears to be affected by orographic blocking* (Fig. 11). The southward upstream deflection has been observed, such as the tracks of 1967 Typhoon Clara and 1971 Typhoon Nadine (Fig. 2a) and the typhoon tracks shown in Fig. 3. *The abrupt increase of the maximum vorticity and contraction of the cyclone*

scale (Figs. 11 and 14c) are caused by the generation of PV associated with the transition from the regime dominated by flow splitting to the regime dominated by wave breaking. The PV generation and regime transition will be discussed later. The abrupt southward movement of surface vorticity center at $Ut/a = 18$ (Fig. 13a) and 3-km vorticity center at $Ut/a = 17$ (Fig. 13c) appears to be due to the adjustment of the primary cyclone to resume its original westward movement and symmetric circulation. The surface and 3-km low centers also move southward upstream (Figs. 13b and 13d). However, unlike the vorticity centers, they move slightly northward over the lee slope and then southward to the original westward track smoothly. The slightly northward movement over the lee slope is due to the influence of adiabatic warming associated with the downslope wind. This adiabatic warming effect is also evidenced by the earlier jump of the surface low to the lee slope, compared with the 3-km low (Figs. 13b and 13d).

The primary cyclone and low centers at both the surface and $\sigma = 3$ km decelerate near the mountain and appear to move much faster or even jump over the mountain peak (Fig. 13). This is consistent with other observational and numerical studies, which indicates that the translational speed of the cyclone tends to increase along with the deflection when it passes over Taiwan (Brand and Blelloch 1974; Wang 1980; Chang 1982; Yeh and Elsberry 1993a). The primary cyclone is decelerated by upstream orographic blocking effects. The surface vorticity and low centers turn southward upstream of the mountain. This is similar to the numerical simulation of Huang and Lin (1997) of a passive vortex over an idealized Taiwan mountain. However, it is different from the numerical simulations of Chang (1982) and Bender et al. (1987), in which the cyclone turns northward upstream. The difference may be due to the cyclone impingement to the central portion of the mountain and the lack of latent heating in the present case. In addition, the mountain sizes are much larger in previous studies (e.g., 240 km $\times$ 480 km in Chang).

Figure 14 shows the time evolution of maximum u, minimum perturbation pressure, maximum vorticity, and maximum PV at the mountain surface. The $u_{\max}$ decreases slightly with time to a value of 27 m s^{-1} at $Ut/a = 11$ and then increases dramatically to its highest value of 31.5 m s^{-1} at $Ut/a = 15$. It then decreases with time. The surface pressure perturbation keeps at about -9 mb until $Ut/a = 8$, increases to its maximum value at $Ut/a = 12$, decreases rapidly to about -9.25 mb at $Ut/a = 16$, and then increases slightly afterward. The maximum vorticity remains at a constant value until about $Ut/a = 9$, increases dramatically to its highest value at $Ut/a = 14$, and then decreases afterward. The sharp increase of the maximum u is associated with that of maximum vorticity. Both of $u_{\max}$ and maximum vorticity increase dramatically when the primary cyclone impinges on the mountain. The earlier weakening of the $p_{\min}$ is caused by the mountain-induced high pressure, and the later strengthening is caused by the adiabatic warming associated with downslope wind on the western slope. The abrupt increase of the vorticity is associated with the PV generation (Fig. 14d). The gradual increase of the PV maximum is due to the adjustment associated with the primary cyclone, which does not contain the vertical velocity initially. The PV at $Ut/a = 0$ in this case (Fig. 14d) is different from that of case V at $Ut/a = 0$ (Fig. 8d) because in the present case it has already adjusted to be lower, mainly due to the decrease of $\partial\theta/\partial z$ (e.g., see Figs. 9b and 9d), during the spinup period of a nondimensional time of 40 before the cyclone injection. Note that the maximum wind speed, 31.5 m s^{-1} (Fig. 14a), is slightly stronger than that in the cyclone-only case (case V, Fig. 8a), 30 m s^{-1}, at $Ut/a = 0$. At $Ut/a = 15$, the rapid increase of the downslope wind appears to be able to help to transport the upstream blocked vorticity to the lee side of the mountain along the center line ($y/a = 0$, see Figs. 12a and 12d). As will be discussed later, the rapid increase of vorticity is mainly caused by new PV generation due to wave breaking associated with the severe downslope wind and internal jump.

Figure 15 shows the regime diagram regarding flow splitting and wave breaking for hydrostatic flow over a mountain based on the horizontal mountain aspect ratio (b/a) and the nondimensional height ($\hat{h} = Nh_0/U$) as proposed by Smith (1989b,c). The inverse Froude number or the nondimensional mountain height is estimated to be about 4 at $(x/a, y/a) = (4, 1)$, where $h_0 = 2.5$ km, $N = 0.01$ s^{-1}, and $U = 10$ ms^{-1}, when the cyclone is located far upstream. This location is chosen for examining the flow regime transition, since it experiences stronger u wind compared to that at $y/a = 0$. The local Froude number reduces to 2.5 at $Ut/a = 5$. According to the regime diagram (Fig. 15a), the flow falls into the regime dominated by flow splitting. The nondimensional mountain height gradually decreases to be about 1.5 at $Ut/a = 13$ when the cyclone is near the mountain (Figs. 15b and 15c). This indicates that the flow shifts gradually from the regime dominated by flow splitting to the regime dominated by wave breaking. The upstream flow shows that the flow splitting is dominant when the cyclone is located upstream (Figs. 10 and 12c), whereas wave breaking is dominant when the cyclone is over the mountain (Figs. 10 and 12f).

To understand the generation for the abrupt increase of the lee vorticity when the primary cyclone approaches the mountain, we have made vorticity and PV budget analyses and present them in the following. The PV budget and vorticity budget formulations can be found in appendices b and c, respectively. Figure 16 shows the vorticity field, local rate of change of vorticity, and advection, stretching, tilting, and mixing and diffusion terms of the vorticity equation at the mountain surface at $Ut/a = 0$. Note that the flow field at the time of cyclone injection is well established because the uniform flow has passed over the mountain for a nondi-

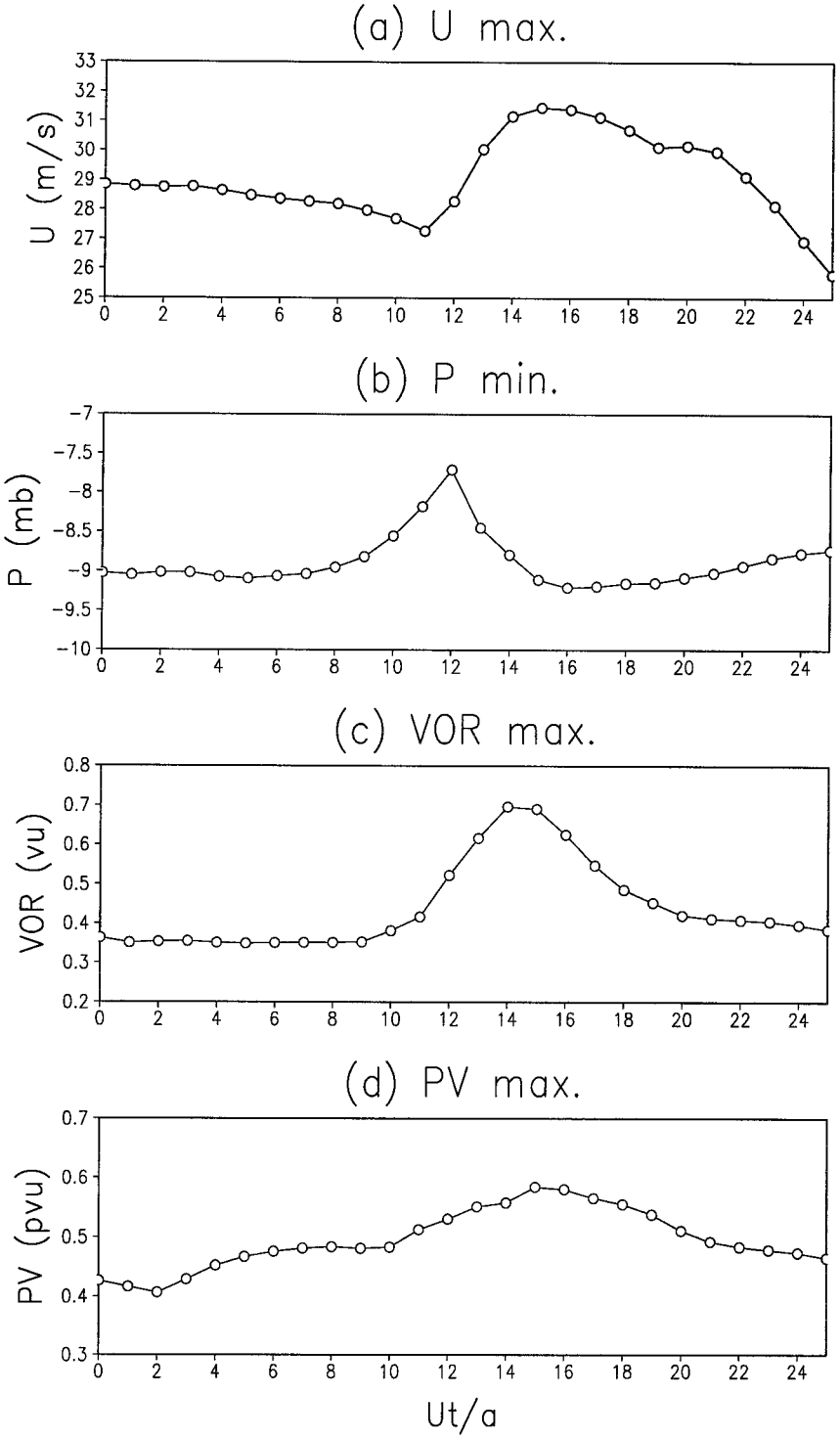

FIG. 14. Same as Fig. 8 except for case MV.

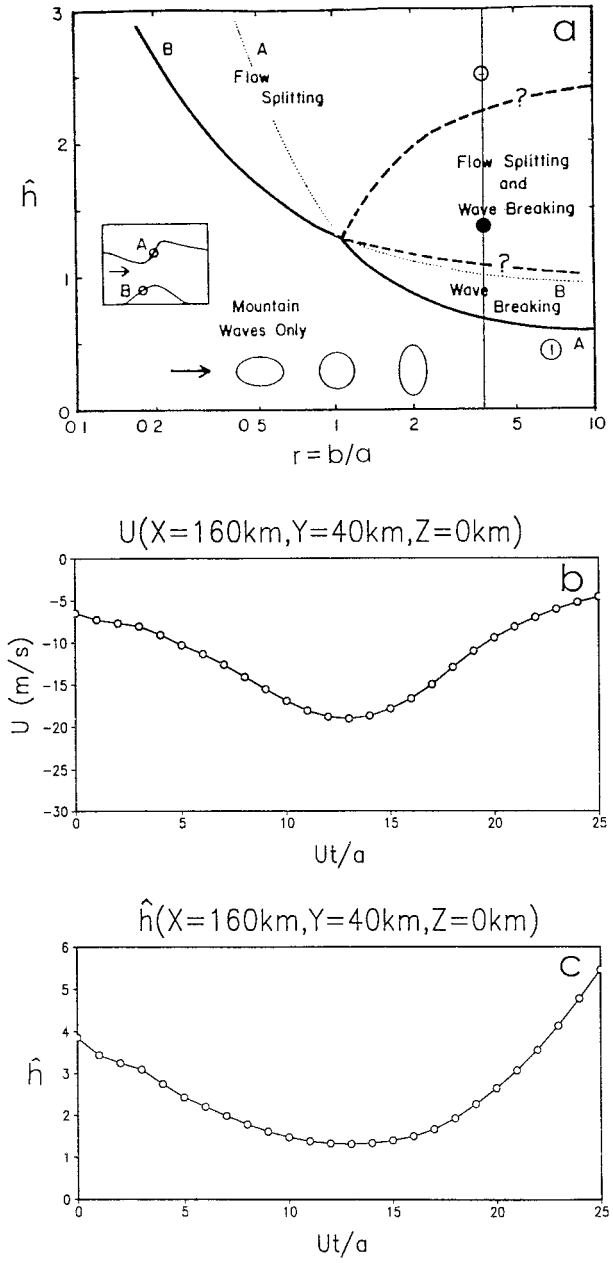

FIG. 15. (a) Regime diagram for hydrostatic flow over a mountain with mountain horizontal aspect ratio (r) and the nondimensional mountain height ($\hat{h}$). Solid curves A and B are linear theory estimates of flow stagnation, suggesting where wave breaking aloft (curve A) and flow splitting (curve B) will begin as $\hat{h}$ increases. The extensions of curves A and B (dotted lines) may be unphysical because the first appearance of a stagnation point could invalidate the linear theory estimates (after Smith 1989b). The flow parameters at $Ut/a = 5$ and 13 are denoted by open and closed circles, respectively, for case MV, (b) u at $(x/a, y/a) = (4, 1)$ on the surface from $Ut/a = 0$ to 25. (c) Same as (b) but with $\hat{h}$.

mensional time of 40. The mixing and diffusion term represents a combined effect of physical subgrid mixing and numerical smoothing (diffusion), which reflects the effects of friction in the interior flow of the real atmosphere, although we have assumed an inviscid fluid flow. Smith and Smith (1995) have proposed a similar argument in a shallow water flow. The PV generated by wave breaking through turbulence is represented by this mixing and diffusion term. The flow field in the vicinity of the mountain in Fig. 16 is similar to the vorticity field under no significant influence of the primary cyclone, because the primary cyclone is still located far upstream—for example, at $x/a = 10$ and $Ut/a = 0$ (Fig. 16a). The vorticity field shows a pair of positive and negative vorticity banners on the lee side, which are associated with the lee vortices generated by the mountain in a low Froude number flow. The Froude number associated with the basic flow is 0.4 in this case. This field is almost identical to that of case M1 (Fig. 4b). At this time, there exists a region of positive vorticity generation over the southern slope and a negative vorticity over the northern slope (Fig. 16b). As can be seen from other terms of the vorticity equation, the contribution of this positive vorticity generation is from both the advection term and the mixing and diffusion term, which counteracted the stretching term. The mixing and diffusion are also responsible for generating PV, based on the PV budget analysis (Fig. 17). The advection term also contributes to the generation of positive PV, but only over the southern slope, which is overcome by the negative PV generation associated with mixing and diffusion. This is similar to that in a nonrotating uniform flow in which the generation of leeside vorticity is produced by PV, as proposed by Smith (1989a). Smith's proposed mechanism of PV generation for lee vorticity is confirmed by numerical modeling study for over a nondimensional time of $O(10)$ to $O(100)$ by Schar and Durran (1997). In the present case, the nondimensional time is 40. Note that the Froude number is 0.4 at this time, so that the flow belongs to the regime dominated by flow splitting (Fig. 15). Thus, the mixing and diffusion come from the westerly flow associated with lee vortices.

When the cyclone approaches the upstream slope, such as $Ut/a = 10$ (Fig. 18a), the vorticity field is very different from that at $Ut/a = 0$ (Fig. 16a). There exist two regions of intense vorticity, one upstream and the other over the southwest slope. Obviously, the upstream vorticity is associated with the primary cyclone. In between these two regions of intense vorticity, there exists a region of strong negative vorticity. As mentioned earlier, this negative vorticity is associated with the southern flank of splitting flow upstream. This also forces a strong vorticity gradient over the eastern slope of the mountain. The region of strong lee vorticity is located to the southwest slope of the mountain range, instead of to the northwest lee slope at earlier time, when no strong influence from the primary cyclone existed (Fig.

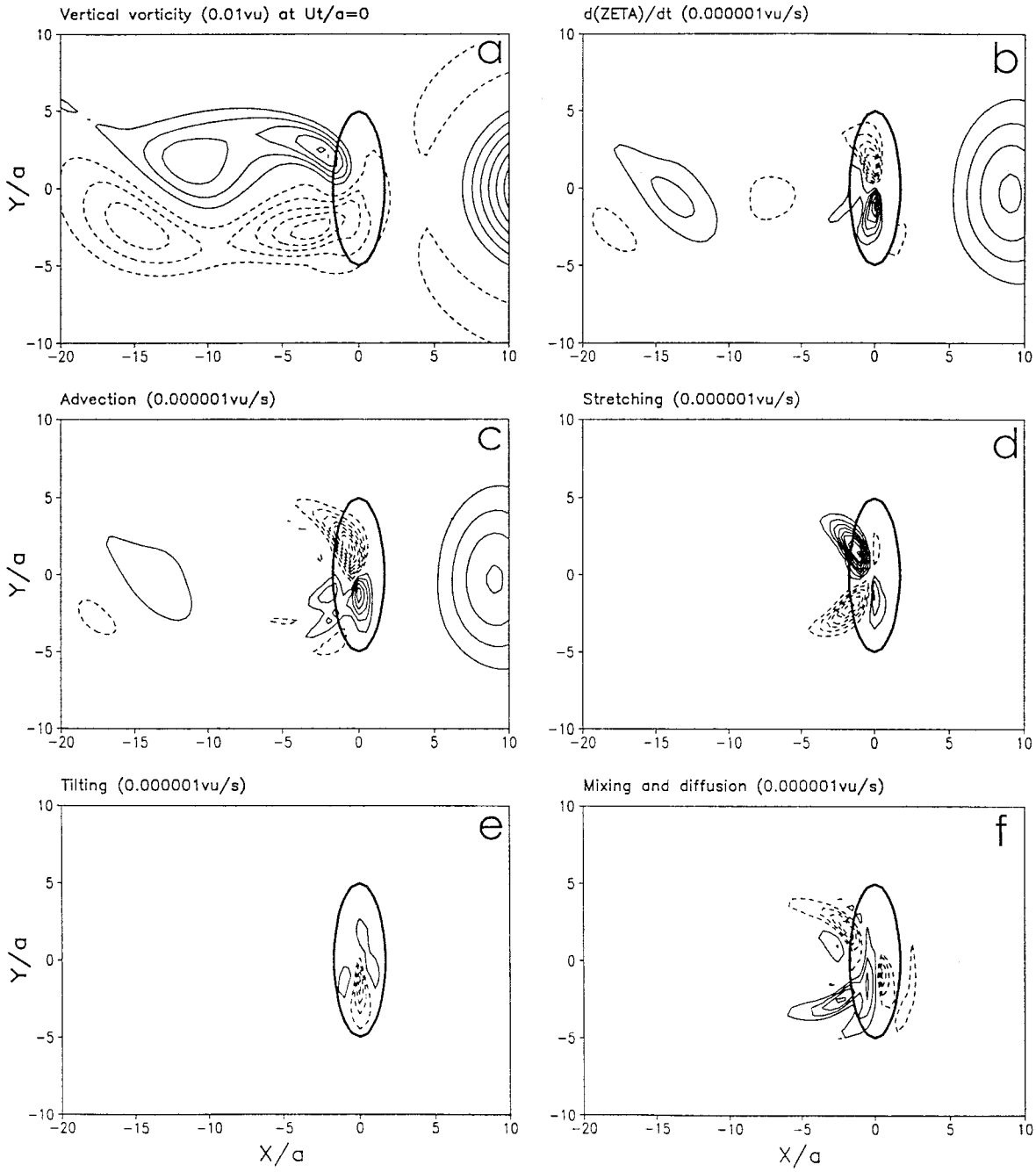

FIG. 16. (a) Vertical vorticity and (b) local rate of change of vorticity ($\partial\zeta/\partial t$) at surface, and different terms in the vorticity equation at $Ut/a = 0$ after cyclone injection: (c) advection, (d) stretching, (e) tilting, and (f) mixing and diffusion. The units are defined as 1 $vu = 10^{-3}$ s^{-1} and 1 $vu/s = 10^{-3}$ s^{-2}. Note the cyclone is injected after the easterly uniform flow over the mountain for a nondimensional time of 40.

16a). The local rate of change of the vertical vorticity (Fig. 18b) indicates that there exist three regions of strong vorticity generation, namely, eastern slope, southwestern slope, and the vorticity banner from the southern tip of the mountain extending northwestward. The upstream vorticity generation is dominated by the advection and stretching (Figs. 18c and 18d). A close inspection of the θ cross section at $y/a = 0$ (Fig. 12c) indicates that the air column does stretch at about $x/a = 2.2$ before it shrinks at about $x/a = 1$. Thus, stretching term is able to produce positive and negative vorticity over the eastern slope. Note that in a stratified uniform

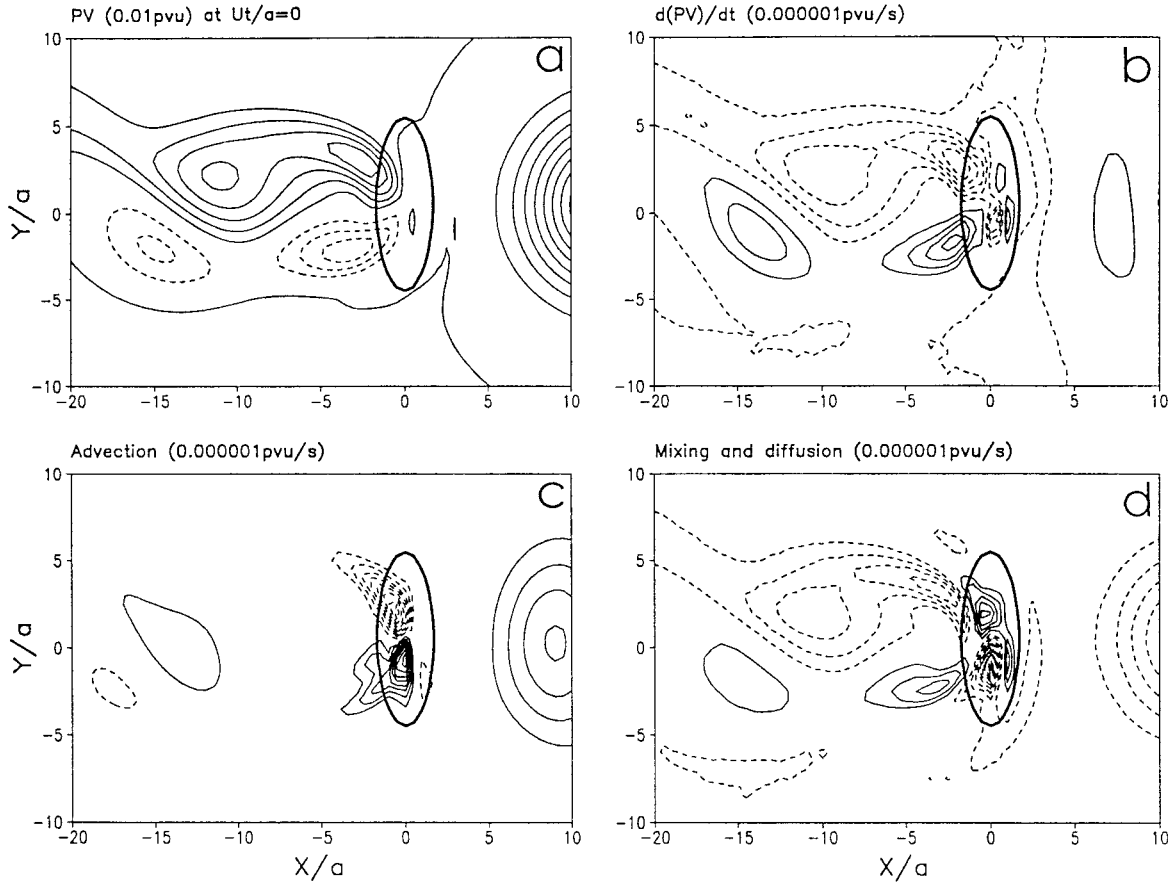

FIG. 17. (a) PV, (b) local rate of change of PV, (c) advection term, and (d) mixing and diffusion term in the PV equation at the surface and $Ut/a = 0$. The units are defined as 1 $pvu = 10^{-6}$ Km^2 s^{-1} kg^{-1} and 1 $pvu/s = 10^{-6}$ Km^2 s^{-2} kg^{-1}.

flow over a mesoscale mountain, the air column does stretch slightly before it shrinks over the mountain peak [Fig. 17 of Smith (1979)]. The positive and negative vorticity banners on the lee are generated by the advection term. This region of positive vorticity production is still occupied by negative vorticity (Fig. 18a). Its effect will become evident at later time, such as $UT/a = 14$ (Fig. 20a). The tilting term appears to play a minor role here (Fig. 18e) and the vorticity production over the mountain peak and southern slope by mixing and diffusion (Fig. 18f) is overcome by the other terms. The PV field (Fig. 19a) shows a similar pattern to the vorticity field (Fig. 18a), whereas the PV generation field (i.e., local rate of change, Fig. 19b) is similar to the vorticity generation field (Fig. 18b). On the lee side, the PV generation field is dominated by the banners of positive and negative PV, which are mainly contributed by the PV advection term (Fig. 19c). A region of strong PV generation due to mixing and diffusion appears on the central lee slope (Fig. 19d), but is overcome by the strong negative PV advection (Fig. 19c) at this time. The PV generation over the eastern slope is mainly due to mixing and diffusion.

When the primary cyclone passes over the mountain peak, such as $Ut/a = 14$ (Fig. 20), the vorticity field is very different from that before passing over the mountain, such as that at $Ut/a = 10$ (Fig. 18). Again, there exist two regions of strong vorticity, a weaker one on upslope and a stronger one over central lee slope. A negative vorticity region is located in between these two positive vorticity regions. The field of local rate of change of vorticity (Fig. 20b) is dominated by a region of very strong positive vorticity generation over the central lee slope and weak banners of positive and negative vorticity extending far downstream. Unlike that at $Ut/a = 10$, the strong vorticity generation over the central lee slope is due to a combination of mixing and diffusion, stretching, and advection. The advection term contributes more on the downstream side of this region of vorticity generation. Again, the tilting term plays a minor role in the lee vorticity generation. The vorticity generation is associated with PV generation, as evidenced by Fig. 21. The PV generation upstream and on the immediate lee of the mountain is dominated by the mixing and diffusion, whereas the PV advection contributes more farther downstream. The effects of mixing and diffusion at this stage are also evidenced by the presence of strong TKE, which is associated with the

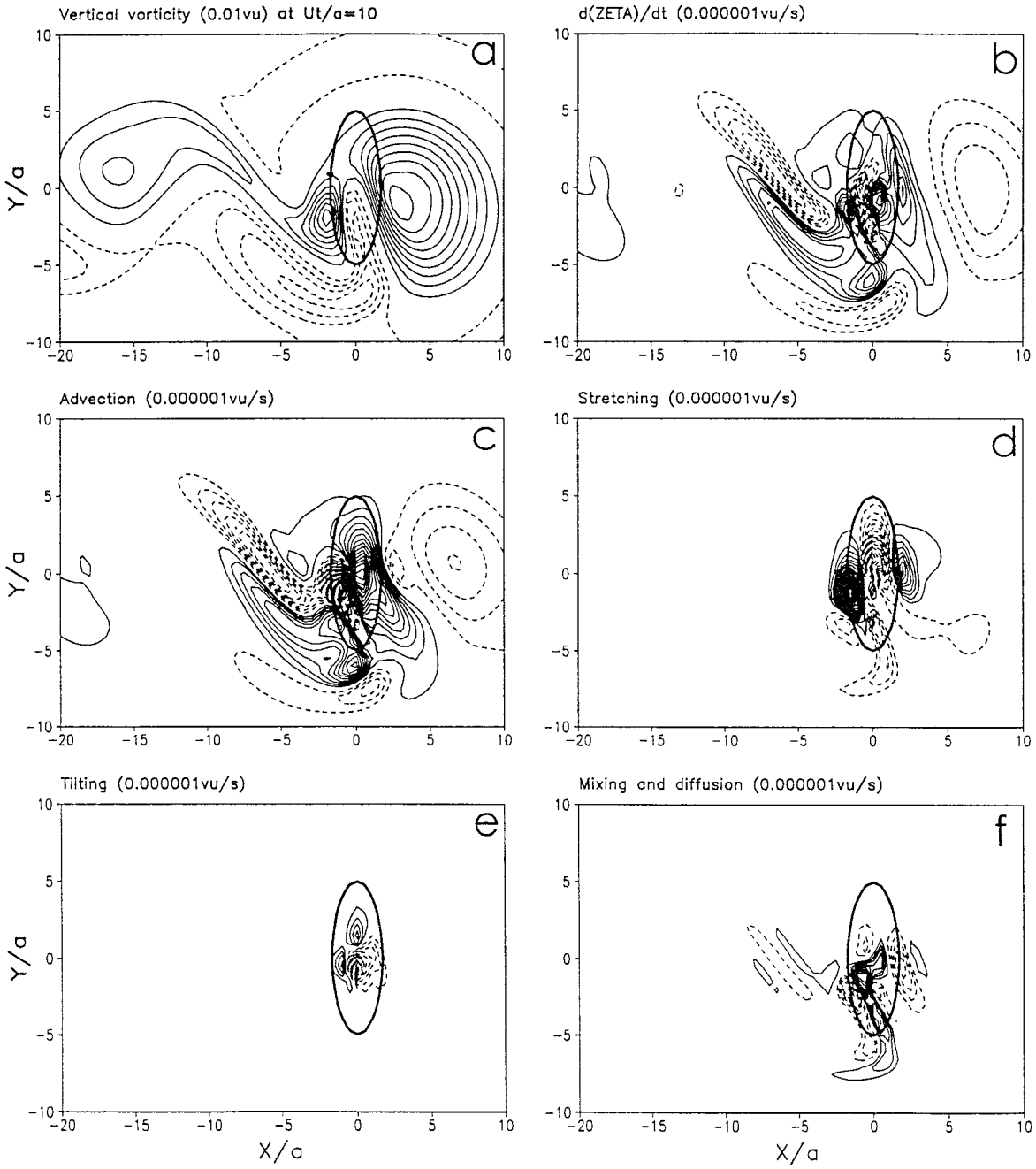

FIG. 18. Same as Fig. 16 except for $Ut/a = 10$.

wave breaking generated by the severe downslope wind and hydraulic jump (Fig. 12f). This analysis is different from Chang's vorticity budget (1982), which showed that vorticity stretching and advection are dominant at this stage. It is uncertain how significant the contribution from mixing and diffusion is in his simulation since it was not calculated. The present result is similar to the downward extension of upper-level vorticity as proposed by Yeh and Elsberry (1993b); however, the abrupt increase of surface vorticity on the lee is now explained by the generation of new PV due to wave breaking.

4. Conclusions and discussions

In this study, a primitive equation numerical model is adopted to investigate the orographic influence on a drifting cyclone over an idealized topography similar to that of Taiwan. The cyclone is in gradient wind balance

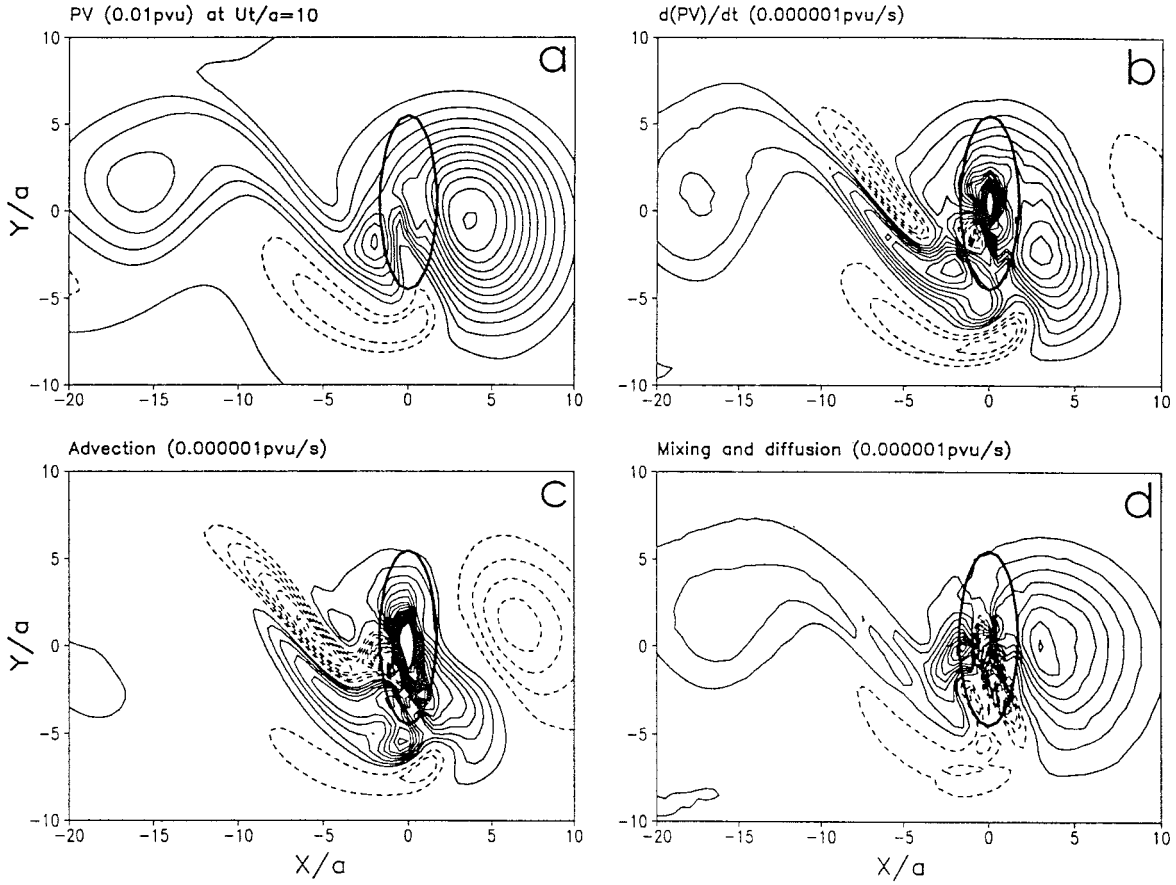

FIG. 19. Same as Fig. 17 except for $Ut/a = 10$.

initially. For a low Froude number, nonrotating stratified uniform flow over an idealized mountain, the flow pattern, vorticity, and PV fields of our numerical simulations are very similar to previous studies. For a rotating stratified uniform flow over an idealized mountain, the symmetry of the positive and negative vorticity is destroyed by the Coriolis force. The pattern of PV field is similar to that of the vertical vorticity field. With a very low Froude number (e.g., Fr = 0.4), the flow belongs to the regime dominated by flow splitting. A pair of positive and negative vorticity centers is generated by the mountain on the lee side and shed downstream. A region of weak positive PV is generated upstream, which is produced by mixing and diffusion associated with the planetary vorticity. The positive vertical vorticity is associated with this PV generation, whereas the negative vorticity over the upslope is produced by column shrinking. With a higher, but still low Froude number (e.g., Fr = 0.8), more air parcels are able to pass over the mountain and produce wave breaking over the lee slope. The flow belongs to the regime dominated by wave breaking. The wave breaking is responsible for PV generation over the lee slope, as shown by the TKE calculation. In addition, at a certain location upstream of the mountain, the local Froude number increases when a cyclone approaches the mountain. This will induce a transition from the regime dominated by flow splitting to the regime dominated by wave breaking.

For a cyclone propagating from the east and impinging on the central portion of the mountain, a northerly surface jet tends to form upstream of the mountain between the primary cyclone and the mountain due to blocking and channeling effects. Two pressure ridges and one trough are also produced, which are associated with hydrostatic response of flow over mountains. These pressure ridges and trough have also been observed for typhoons over Taiwan (Wang 1980). When the cyclone approaches the mountain, the low-level vorticity and low pressure center decelerate and turn southward upstream of the mountain due to orographic blocking. This type of southward upstream deflection has also been observed for typhoons crossing the Central Mountain Range of Taiwan (Wang 1980). At the same time, the upstream low-level vorticity is blocked by the mountain. The present result is similar to the downward extension of upper-level vorticity as proposed by Yeh and Elsberry (1993b), however, the abrupt increase of surface vorticity and the contraction of cyclone scale on the lee side are now explained by the generation of new PV due to wave breaking as-

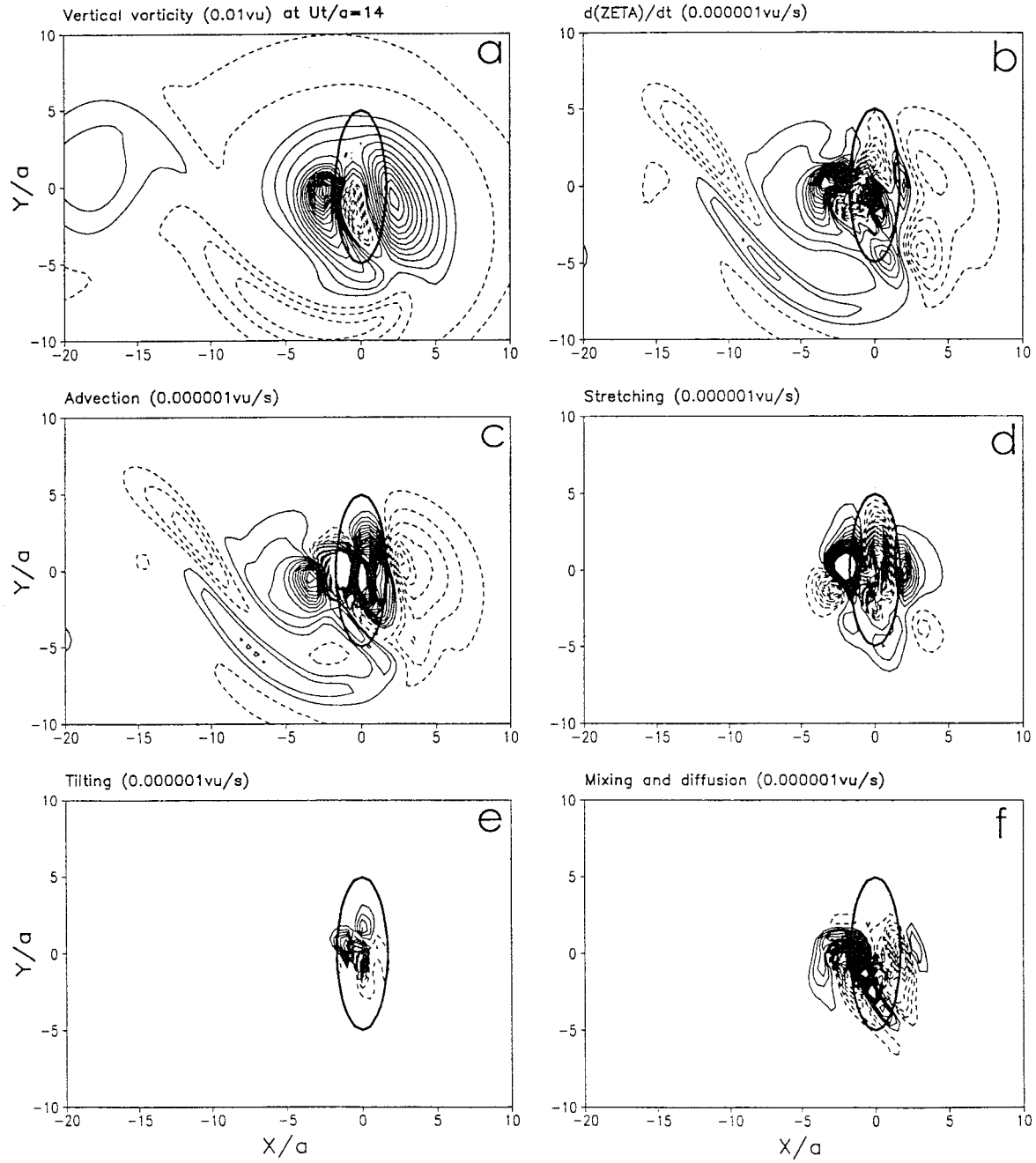

FIG. 20. Same as Fig. 16 except for $Ut/a = 14$.

sociated with the severe downslope wind and hydraulic jump. The generation of this new PV is evidenced by the dominance of mixing and diffusion term, which here is equivalent to friction in the real atmosphere, in the vorticity and PV budgets, and the evolution of the nondimensional mountain height (inverse Froude number) in the regime diagram proposed by Smith (1989b,c). At this stage, the cyclone and low pressure centers appear to accelerate or jump over the mountain. At the same time, the surface low shifts to the south of the original westward track, which is primarily influenced by strong adiabatic warming associated with the downslope wind. The primary surface cyclone then resumes its original westward movement and symmetric circulation on the lee side once it moves away from the mountain. During this adjustment process, the surface and 3-km vorticity centers appear to move southward abruptly. The low centers move slightly northward over the lee slope and then southward to its original westward track smoothly. The northward

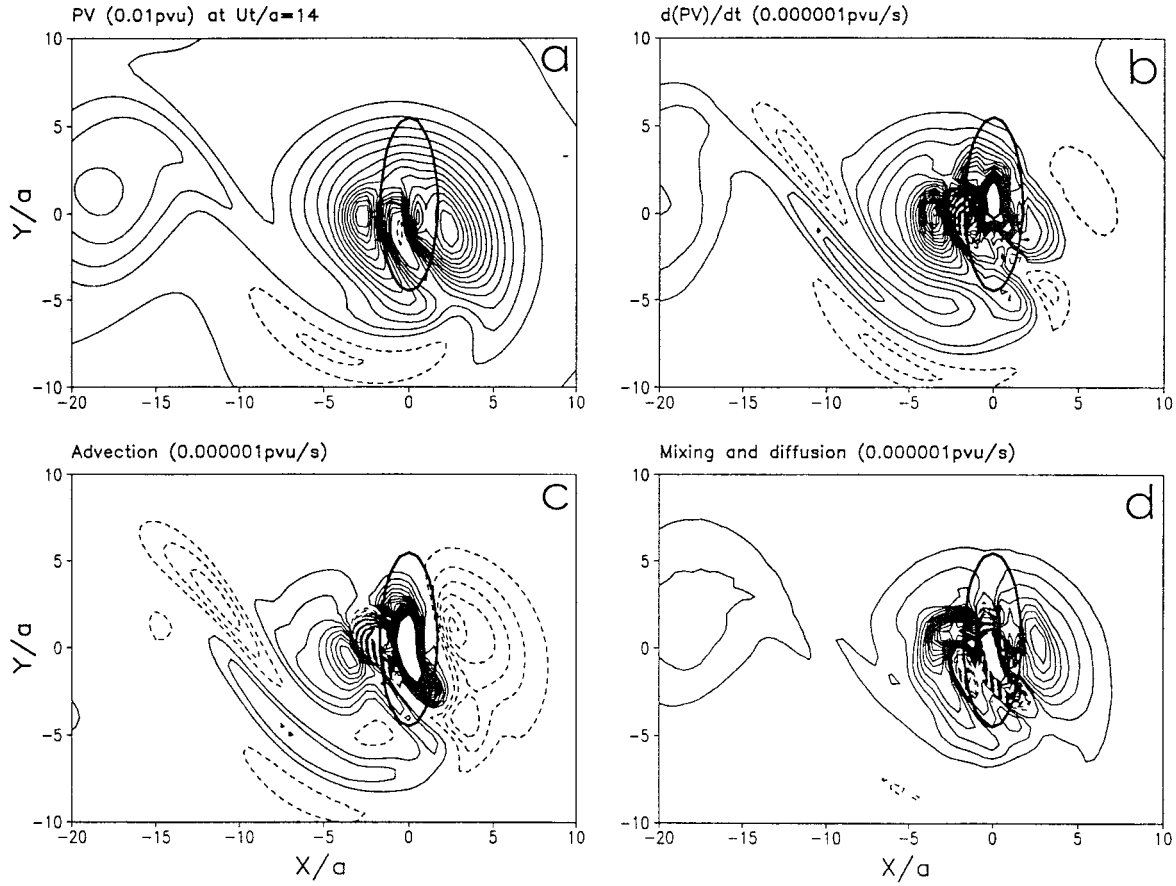

FIG. 21. Same as Fig. 17 except for $Ut/a = 14$.

movement of the surface low over the lee slope is due to the influence of adiabatic warming associated with the downslope wind. The deflection of the cyclone and low pressure centers at midlevels (e.g., $\sigma = 3$ km) are similar to those at the surface.

When the cyclone is located far upstream of the mountain, the vorticity budget analysis indicates that the contribution of the positive vorticity production over the southern lee slope is from both the advection term and the mixing and diffusion term, which counteract the streching term. The mixing and diffusion are also responsible for generating the PV, based on PV budget analysis. When the cyclone approaches the mountain, there exists three regions of strong local vorticity production, namely, eastern slope, western slope, and the vorticity banner extending from the southern tip of the mountain to northwest. The upslope vorticity production is dominated by the advection and stretching. The vorticity banner is produced by the vorticity advection. The PV generation field is similar to the vorticity generation field. On the lee side, the PV generation is mainly contributed by the PV advection. When the cyclone passes over the mountain peak, the local vorticity generation field is dominated by a region of very strong positive vorticity generation over the central lee slope and weak banners of positive and negative vorticity. Unlike that before the cyclone passes over the mountain, the strong vorticity generation over the central lee slope is due to a combination of mixing and diffusion, stretching, and advection. The PV generation on the lee side of the mountain is dominated by the mixing and diffusion, while the advection contributes more on the downstream side. This finding is similar to that found by Smith and Smith (1995) in the context of shallow water theory. However, in a stratified flow, the transition is from regime dominated by flow splitting to regime dominated by wave breaking. On the other hand, in a shallow water system, the transition is from irrotational flow to flow over the mountain with wakes.

In this study, we have made several assumptions, which include an inviscid and dry atmosphere, relatively larger basic flow, lack of fine resolution over the steep mountain slope, hydrostatic approximation, etc. The frictional effects in the planetary boundary layer tend to reduce the flow speed near the surface, which will then reduce the local Froude number near surface accordingly. This will be addressed along with a more complete discussion of sensitivity tests, such as weaker basic flow, impinging angle, larger cyclone, and landing locations, etc., in a separate study. The addition of latent heating

may strongly influence the cyclone track and its circulation probably due to a much stronger upward motion over the upslope. Besides, the cyclone propagation speed will be influenced by the addition of latent heating, instead of simply drifting with the basic wind. If a weaker basic flow is considered, then the Froude number will be decreased. This will influence the flow pattern and cyclone track farther upstream, as found in Bender et al. (1987). To resolve the steep terrain of the Taiwan topography, a nonhydrostatic model may be needed.

Acknowledgments. Discussions with Dr. R. B. Smith, Mr. S.-T. Wang, Dr. T.-C. Yeh, Dr. C.-C. Wu, and Dr. S. Chang are highly appreciated. The authors would also like to thank Dr. R. P. Weglarz for proofreading the manuscript. Comments made by Dr. M. A. Bender and other reviewers have greatly improved the quality of this paper. This work is supported by the NSF Grant #ATM-9224595. Part of the computations was performed on the NCSC supercomputer and IBM FOAM^{v} workstations at NCSU.

APPENDIX A

Vortex Initialization

The momentum equations in a two-dimensional, inviscid, incompressible, and Boussinesq fluid are given by

$$\frac{\partial u}{\partial t} + u\frac{\partial u}{\partial x} + v\frac{\partial u}{\partial y} - f_0 v = -\frac{\partial \pi}{\partial x} \tag{A1}$$

$$\frac{\partial v}{\partial t} + u\frac{\partial v}{\partial x} + v\frac{\partial v}{\partial y} - f_0 u = -\frac{\partial \pi}{\partial y} \tag{A2}$$

$$\frac{\partial u}{\partial x} + \frac{\partial v}{\partial y} = 0, \tag{A3}$$

where $\pi = p'/\rho_0$. Adding x derivative of Eq. (A1) and y derivative of Eq. (A2), one can obtain a Poisson equation for π; that is,

$$\nabla_h^2 \pi = f_0 \varsigma + 2\left(\frac{\partial u}{\partial x}\frac{\partial v}{\partial y} - \frac{\partial v}{\partial x}\frac{\partial u}{\partial y}\right). \tag{A4}$$

In addition, if a streamfunction is defined as

$$u = -\frac{\partial \psi}{\partial y}, \qquad v = \frac{\partial \psi}{\partial x}, \tag{A5}$$

which satisfy the continuity equation (A3), it gives the relationship between vertical vorticity and streamfunction; that is,

$$\nabla_h^2 \psi = \varsigma. \tag{A6}$$

The vortex initialization procedures are as follows:

1) Obtain the vertical vorticity field from the two-dimensional wind of Eq. (19).
2) Solve Eq. (A6) to obtain the streamfunction.
3) Obtain u and v fields with the streamfunction and Eq. (A5). Thus, the new velocity field is nondivergent.
4) Solve Eq. (A4) to obtain the perturbation pressure field.
5) Use the hydrostatic Eq. (3) to obtain the potential temperature field.
6) Superimpose the initialized vortex on the environmental fields.

In (2) and (4), the Gauss–Seidal iteration method is used to solve a Poisson equation with the zero-gradient boundary condition. The above procedure is similar to that adopted by Huang and Lin (1997).

APPENDIX B

The Potential Vorticity (PV) Equation

The PV is defined as

$$\mathrm{PV} \equiv \frac{1}{\rho_0}(\boldsymbol{\xi} + f_0\mathbf{k}) \cdot \nabla\theta, \tag{B1}$$

where $\boldsymbol{\zeta}$ is the vorticity vector. In the absence of diabatic heating, the PV conservation equation is given by

$$\frac{\partial(\mathrm{PV})}{\partial t} + \mathbf{V} \cdot \nabla(\mathrm{PV}) = \frac{1}{\rho_0}[\nabla\theta \cdot (\nabla \times \mathbf{F})], \tag{B2}$$

where $\mathbf{V}$ is the velocity vector, and $\mathbf{F}$ the frictional force, and $\dot{\theta}$ the diabatic source term. In the present study, $\dot{\theta}$ represents the heat diffusion by subgrid turbulent mixing and numerical smoothing in the absence of latent heating or radiative heating. Two terms of the left-hand side in Eq. (B1) represent the local change of rate of PV and PV advection by velocity field, respectively. The frictional PV generation term of the right-hand side in Eq. (B2) can be expressed as

$$\begin{aligned}
&\nabla\theta \cdot (\nabla \times \mathbf{F}) \\
&\quad = -\frac{\partial F_v}{\partial z}\frac{\partial \theta}{\partial x} + \frac{\partial F_u}{\partial z}\frac{\partial \theta}{\partial y} + \left(\frac{\partial F_v}{\partial x} - \frac{\partial F_u}{\partial y}\right)\frac{\partial \theta}{\partial z} \\
&\qquad - \frac{\partial S_v}{\partial z}\frac{\partial \theta}{\partial x} + \frac{\partial S_u}{\partial z}\frac{\partial \theta}{\partial y} + \left(\frac{\partial S_v}{\partial x} - \frac{\partial S_u}{\partial y}\right)\frac{\partial \theta}{\partial z} \\
&\qquad + \xi\frac{\partial F_\theta}{\partial x} + \eta\frac{\partial F_\theta}{\partial y} + \varsigma\frac{\partial F_\theta}{\partial z} + f_0\frac{\partial F_\theta}{\partial z} \\
&\qquad + \xi\frac{\partial S_\theta}{\partial x} + \eta\frac{\partial S_\theta}{\partial y} + \varsigma\frac{\partial S_\theta}{\partial z} + f_0\frac{\partial S_\theta}{\partial z},
\end{aligned} \tag{B3}$$

where S_u, S_v, and S_θ are the numerical diffusion (smoothing) terms for u, v, and θ, and ξ, η, and ζ the x-, y-, and z- component of relative vorticity, respectively. Here F_u, F_v, and F_θ are the vertical turbulent mixing terms for u, v, and θ, respectively; that is,

$$F_u = \frac{\partial(-\overline{u'w'})}{\partial z}, \qquad F_v = \frac{\partial(-\overline{v'w'})}{\partial z}, \qquad \text{and}$$

$$F_\theta = \frac{\partial(-\overline{\theta'w'})}{\partial z}. \tag{B4}$$

The *PV* conservation equation on terrain-following coordinate can be expressed as

$$\frac{\partial(PV)}{\partial t} + \frac{u}{H}\left\{\frac{\partial[H(PV)]}{\partial x} + \frac{\partial[G(PV)]}{\partial \sigma}\right\} + \frac{v}{H}\left\{\frac{\partial[H(PV)]}{\partial y} + \frac{\partial[J(PV)]}{\partial \sigma}\right\} + \frac{w}{H}\frac{\partial(PV)}{\partial \sigma}$$
$$= -\frac{1}{H^2}\frac{\partial F_v}{\partial \sigma}\left[\frac{\partial(H\theta)}{\partial x} + \frac{\partial(G\theta)}{\partial \sigma}\right] + \frac{1}{H^2}\frac{\partial F_u}{\partial \sigma}\left[\frac{\partial(H\theta)}{\partial y} + \frac{\partial(J\theta)}{\partial \sigma}\right] + \frac{1}{H^2}\frac{\partial \theta}{\partial \sigma}\left[\frac{\partial(HF_v)}{\partial x} + \frac{\partial(GF_v)}{\partial \sigma} - \frac{\partial(HF_u)}{\partial y} - \frac{\partial(JF_u)}{\partial \sigma}\right]$$
$$- \frac{1}{H^2}\frac{\partial S_v}{\partial \sigma}\left[\frac{\partial(H\theta)}{\partial x} + \frac{\partial(G\theta)}{\partial \sigma}\right] + \frac{1}{H^2}\frac{\partial S_u}{\partial \sigma}\left[\frac{\partial(H\theta)}{\partial y} + \frac{\partial(J\theta)}{\partial \sigma}\right] + \frac{1}{H^2}\frac{\partial \theta}{\partial \sigma}\left[\frac{\partial(HS_v)}{\partial x} + \frac{\partial(GS_v)}{\partial \sigma} - \frac{\partial(HS_u)}{\partial y} - \frac{\partial(JS_u)}{\partial \sigma}\right]$$
$$+ \frac{\xi}{H}\left[\frac{\partial(HF_\theta)}{\partial x} + \frac{\partial(GF_\theta)}{\partial \sigma}\right] + \frac{\eta}{H}\left[\frac{\partial(HF_\theta)}{\partial y} + \frac{\partial(JF_\theta)}{\partial \sigma}\right] + \frac{\varsigma}{H}\frac{\partial F_\theta}{\partial \sigma} + \frac{f_0}{H}\frac{\partial F_\theta}{\partial \sigma} + \frac{\xi}{H}\left[\frac{\partial(HS_\theta)}{\partial x} + \frac{\partial(GS_\theta)}{\partial \sigma}\right]$$
$$+ \frac{\eta}{H}\left[\frac{\partial(HS_\theta)}{\partial y} + \frac{\partial(JS_\theta)}{\partial \sigma}\right] + \frac{\varsigma}{H}\frac{\partial S_\theta}{\partial \sigma} + \frac{f_0}{H}\frac{\partial S_\theta}{\partial \sigma}. \quad \text{(B5)}$$

APPENDIX C

The Vertical Vorticity Equation

Based on the governing equations, vertical vorticity conservation equation is given by

$$\frac{\partial \varsigma}{\partial t} + \mathbf{V}\cdot\nabla\varsigma = -(\varsigma + f_0)\left(\frac{\partial u}{\partial x} + \frac{\partial v}{\partial y}\right) + \left(\xi\frac{\partial w}{\partial x} + \eta\frac{\partial w}{\partial y}\right) + \left(\frac{\partial F_v}{\partial x} - \frac{\partial F_u}{\partial y}\right) + \left(\frac{\partial S_v}{\partial x} - \frac{\partial S_u}{\partial y}\right). \quad \text{(C1)}$$

Note that under hydrostatic assumption the horizontal components of vorticity are defined as

$$\xi = -\frac{\partial v}{\partial z} \quad \text{and} \quad \eta = \frac{\partial u}{\partial z}. \quad \text{(C2)}$$

Two terms of the left-hand side in Eq. (C1) represent the local change of rate of vertical vorticity and vorticity advection by velocity field, respectively. The terms of the right-hand side in Eq. (C1) are the vertical vorticity productions due to stretching, tilting, turbulent mixing, and numerical diffusion, respectively.

The vertical vorticity conservation equation on terrain-following coordinate can be expressed as

$$\frac{\partial \varsigma}{\partial t} + \frac{u}{H}\left[\frac{\partial(H\varsigma)}{\partial x} + \frac{\partial(G\varsigma)}{\partial \sigma}\right] + \frac{v}{H}\left[\frac{\partial(H\varsigma)}{\partial y} + \frac{\partial(J\varsigma)}{\partial \sigma}\right] + \frac{w}{H}\frac{\partial \varsigma}{\partial \sigma}$$
$$= -\frac{(\varsigma + f_0)}{H}\left[\frac{\partial(Hu)}{\partial x} + \frac{\partial(Gu)}{\partial \sigma} + \frac{\partial(Hv)}{\partial y} + \frac{\partial(Jv)}{\partial \sigma}\right]$$
$$+ \frac{\xi}{H}\left[\frac{\partial(Hw)}{\partial x} + \frac{\partial(Gw)}{\partial \sigma}\right] + \frac{\eta}{H}\left[\frac{\partial(Hw)}{\partial y} + \frac{\partial(Jw)}{\partial \sigma}\right]$$
$$+ \frac{1}{H}\left[\frac{\partial(HF_v)}{\partial x} + \frac{\partial(GF_v)}{\partial \sigma} - \frac{\partial(HF_u)}{\partial y} - \frac{\partial(JF_u)}{\partial \sigma}\right]$$
$$+ \frac{1}{H}\left[\frac{\partial(HS_v)}{\partial x} + \frac{\partial(GS_v)}{\partial \sigma} - \frac{\partial(HS_u)}{\partial y} - \frac{\partial(JS_u)}{\partial \sigma}\right]. \quad \text{(C3)}$$

REFERENCES

Bender, M. A., R. E. Tuleya, and Y. Kurihara, 1985: A numerical study of the effect of a mountain range on a landfalling tropical cyclone. *Mon. Wea. Rev.*, **113,** 567–582.

——, ——, and ——, 1987: A numerical study of the effect of island terrain on tropical cyclones. *Mon. Wea. Rev.*, **115,** 130–155.

Bougeault, P., and P. Lacarrere, 1989: Parameterization of orography-induced turbulence in a mesobeta-scale model. *Mon. Wea. Rev.*, **117,** 1872–1890.

Brand, S., and J. W. Blelloch, 1973: Changes in the characteristics of typhoons crossing the Philippines. *J. Appl. Meteor.*, **12,** 104–109.

——, and ——, 1974: Changes in the characteristics of typhoons crossing the island of Taiwan. *Mon. Wea. Rev.*, **102,** 708–713.

——, J. C. Herb, J. C. Woo, J. J. Lou, and M. Danard, 1982: Mesoscale effects of topography on tropical cyclone–associated surface winds. *Pap. Meteor. Res.*, **5,** 37–49.

Chan, J. C.-L., 1984: An observational study of the physical processes responsible for tropical cyclone motion. *J. Atmos. Sci.*, **41,** 1036–1048.

Chang, S. W.-J., 1982: The orographic effects induced by an island mountain range on propagating tropical cyclones. *Mon. Wea. Rev.*, **110,** 1255–1270.

Clark, T. L., 1977: A small scale dynamic model using a terrain-following coordinate transformation. *J. Comput. Phys.*, **24,** 186–215.

Crook, N. A., T. L. Clark, and M. W. Moncrieff, 1990: The Denver cyclone. Part I: Generation in low Froude number flow. *J. Atmos. Sci.*, **47,** 2725–2742.

Gal-Chen, T., and R. C. J. Sommerville, 1975: On the use of a coordinate transformation for the solution of the Navier–Stokes equations. *J. Comput. Phys.*, **17,** 209–228.

Haltiner, G. J., and R. T. Williams, 1980: *Numerical Prediction and Dynamic Meteorology.* 2d ed. John Wiley and Sons, 477 pp.

Han, J., 1998: Large eddy simulations of aircraft wake vortices in a

homogeneous atmospheric turbulence. Ph.D. dissertation, North Carolina State University, 162 pp.
Hebert, P. J., 1980: Atlantic hurricane season of 1979. *Mon. Wea. Rev.,* **108,** 973–990.
Huang, C.-Y., and Y.-L. Lin, 1997: The evolution of mesoscale vortex impinging on symmetric topography. Proc. Taiwan National Science Council, Part A, 21, 285–309. [Available from Dr. Y.-L. Lin, Dept. of Marine, Earth, and Atmospheric Sciences, North Carolina State University, Raleigh, NC 27695-8208.]
Hwang, R. R., H. P. Pao, and S. T. Wang, 1977: Laboratory study of the effects on typhoons when encountering the mountains of Taiwan Island. *Acad. Sin.*
Kintanar, R. L., and L. A. Amadore, 1974: Typhoon climatology in relation to weather modification activities. WMO, No. 408. [Available from WMO Secretariat, CP 5, CH-1211, Geneva 20, Switzerland.]
Klemp, J. B., and D. R. Durran, 1983: An upper boundary condition permitting internal gravity wave radiation in numerical mesoscale models. *Mon. Wea. Rev.,* **111,** 430–444.
Lacser, A., and S. P. S. Arya, 1986: A comparative assessment of mixing-length parameterizations in the stably stratified nocturnal boundary layer (NBL). *Bound.-Layer Meteor.,* **36,** 53–70.
Lin, Y.-L., N.-H. Lin, and R. P. Weglarz, 1992: Numerical modeling studies of lee mesolows, mesovortices, and mesocyclones with application to the formation of Taiwan mesolows. *Meteor. Atmos. Phys.,* **49,** 43–67.
Olafsson, H., and P. Bougeault, 1996: Nonlinear flow past an elliptic mountain ridge. *J. Atmos. Sci.,* **53,** 2465–2489.
Orlanski, I., 1976: A simple boundary condition for unbounded hyperbolic flows. *J. Comput. Phys.,* **21,** 251–269.
Schar, C., and R. B. Smith, 1993a: Shallow-water flow past isolated topography. Part I: Vorticity production and wake formation. *J. Atmos. Sci.,* **50,** 1373–1400.
——, and ——, 1993b: Shallow-water flow past isolated topography. Part II: Transition to vortex shedding. *J. Atmos. Sci.,* **50,** 1401–1412.
——, and D. R. Durran, 1997: Vortex formation and vortex shedding in continuously stratified flows past isolated topography. *J. Atmos. Sci.,* **54,** 534–554.
Shapiro, R., 1970: Smoothing, filtering, and boundary effects. *Rev. Geophys. Space Phys.,* **8,** 359–387.
Smith, R. B., 1979: The influence of mountains on the atmosphere. *Advances in Geophysics,* Vol. 21, Academic Press, 87–230.
——, 1980: Linear theory of stratified hydrostatic flow past an isolated mountain. *Tellus,* **32,** 348–364.
Smith, R. B., 1989a: Comments on ''Low Froude number flow past three-dimensional obstacles. Part I: Baroclinically generated lee vortices.'' *J. Atmos. Sci.,* **46,** 3611–3613.
——, 1989b: Mountain-induced stagnation points in hydrostatic flow. Tellus, **41A,** 270–274.
——, 1989c: Hydrostatic airflow over mountains. *Advances in Geophysics,* Vol. 31, Academic Press, 1–41.
——, and D. F. Smith, 1995: Pseudoinviscid wake formation by mountains in shallow-water flow with a drifting vortex. *J. Atmos. Sci.,* **52,** 436–454.
——, A. C. Gleason, and P. A. Gluhosky, 1997: The wake of St. Vincent. *J. Atmos. Sci.,* **54,** 606–623.
Smolarkiewicz, P. K., and R. Rotunno, 1989: Low Froude number flow past three-dimensional obstacles. Part I: Baroclinically generated lee vortices. *J. Atmos. Sci.,* **46,** 1154–1164.
Sun, W.-Y., J. D. Chern, C.-C. Wu, and W.-R. Hsu, 1991: Numerical simulation of mesoscale circulation in Taiwan and surrounding area. *Mon. Wea. Rev.,* **119,** 2558–2573.
Wang, S.-T., 1980: Prediction of the movement and strength of typhoons in Taiwan and its vicinity (in Chinese). Res. Rep. 108, Taiwan National Science Council, Taipei, Taiwan, 100 pp.
——, 1989: The characteristics of typhoon wind field and methods of gust wind prediction in Taiwan. Taiwan National Science Council Tech. Rep. 77–58, Taipei, Taiwan, 94 pp.
Yeh, T.-C., and R. L. Elsberry, 1993a: Interaction of typhoons with the Taiwan orography. Part I: Upstream track deflections. *Mon. Wea. Rev.,* **121,** 3193–3212.
——, and ——, 1993b: Interaction of typhoons with the Taiwan topography. Part II: Continuous and discontinuous tracks across the island. *Mon. Wea. Rev.,* **121,** 3213–3233.